Structure of a Force-Conveying Cadherin Bond Essential for Inner-Ear Mechanotransduction

Structure of a Force-Conveying Cadherin Bond Essential for Inner-Ear Mechanotransduction

Marcos Sotomayor[ß], Wilhelm A. Weihofen[*†], Rachelle Gaudet[*‡], David P. Corey[ß‡]

[ß] Howard Hughes Medical Institute and Department of Neurobiology,
Harvard Medical School, Boston, MA 02115, USA.
* Department of Molecular and Cellular Biology, Harvard University, Cambridge, MA 02138, USA.
† Present address: Novartis Institutes for BioMedical Research, Cambridge, MA 02139, USA.
‡ Corresponding authors: dcorey@hms.harvard.edu; gaudet@mcb.harvard.edu.

Running Title: Structures and Simulations of Tip-Link Cadherins

August 2012

Hearing and balance use hair cells in the inner ear to transform mechanical stimuli into electrical signals[1]. Mechanical force from sound waves or head movements is conveyed to hair-cell transduction channels by tip links[2,3], fine filaments formed by two atypical cadherins: protocadherin-15 and cadherin-23[4,5]. These two proteins are products of deafness genes[6-10] and feature long extracellular domains that interact tip-to-tip[5,11] in a Ca^{2+}-dependent manner. However, the molecular architecture of the complex is unknown. Here we combine crystallography, molecular dynamics simulations, and binding experiments to characterize the cadherin-23 and protocadherin-15 bond. We find a unique cadherin interaction mechanism, with the two most N-terminal cadherin repeats (EC1+2) of each protein interacting to form an overlapped, antiparallel heterodimer. Simulations predict that this tip-link bond is mechanically strong enough to resist forces in hair cells. In addition, the complex becomes unstable upon Ca^{2+} removal due to increased flexure of Ca^{2+}-free cadherin repeats. Finally, we use structures and biochemical measurements to understand molecular mechanisms by which deafness mutations disrupt tip-link function. Overall, our results shed light on the molecular mechanics of hair-cell sensory transduction and on new interaction mechanisms for cadherins, a large protein family implicated in tissue and organ morphogenesis[12,13], neural connectivity[14], and cancer[15].

Hair cell mechanotransduction happens within each bundle of stereocilia (Fig. 1a), which is deflected by mechanical stimulation[1]. Deflection results in tension applied to tip links, protein filaments linking the tip of each stereocilium to its tallest neighbour[2,3]. The tip links, acting in series with an elastic "gating spring," pull open transduction channels[1]. Recently, protocadherin-15 and cadherin-23, which feature exceptionally long extracellular domains with 11 and 27 extracellular cadherin (EC) repeats (Fig. 1b), were shown to form the tip link[4,5]. To elucidate the tip-link heterophilic molecular bond between protocadherin-15 and cadherin-23, we determined the crystallographic structure of their interacting N-termini (Fig. 1c; results summary in Supplementary Fig. 1). Size exclusion chromatography (SEC) of co-refolded protein fragments comprising the EC1+2 repeats of protocadherin-15 and EC1+2 of cadherin-23 (referred to here as pcdh-15 and cdh-23, respectively) showed a monodisperse peak with the two protein fragments interacting in solution (Supplementary Fig. 2a). The complex crystallized in two packing arrangements and two independent models were fully refined (S1a-S1b and S2, respectively; Supplementary Table 1 and Supplementary Fig. 3).

The structures show that pcdh-15 and cdh-23 form an overlapping and antiparallel heterodimer (pcdh-15+cdh-23; Figs 1c, f and g). The interaction resembles an "extended handshake" and involves repeats EC1 *and* EC2 from both proteins. The overall fold of pcdh-15 and cdh-23 matched the well-known Greek-key motif of classical cadherins (Supplementary Fig. 4). As expected, three Ca^{2+} ions are found in a canonical arrangement (sites 1, 2, and 3) at the linker region between repeats EC1 and EC2 of each protein (Fig. 1c,e). However, several novel structural features within pcdh-15 and cdh-23 enable the handshake interaction.

Pcdh-15 has an elongated N-terminus clamped by an intramolecular disulfide bond (Fig. 1d), which is followed by a conserved RXGPP motif that forms a rigid and bulky loop (Supplementary Fig. 5a&b). This RXGPP loop, within strand A of protocadherin-15 EC1, is tucked against the narrow wrist of the adjacent cdh-23's linker region (Fig. 1c). Similarly, cdh-23 has an elongated N-terminus, stabilized at the tip by Ca^{2+}-binding site 0[16,17], which is followed by a bulky 3_{10} helix within strand A that sits at the narrow wrist

of the adjacent pcdh-15's linker (Fig. 1c). Thus, the pcdh-15+cdh-23 interface exploits unique structural protrusions within strand A of each EC1 repeat, which in turn are stabilized by a disulfide bond and a Ca^{2+}-binding site and lead to two main areas of interaction described below.

The pcdh-15+cdh-23 heterophilic interface differs from the strand-exchanged or X-dimer homophilic interfaces of classical cadherins[18-20]. Furthermore, this interface is not directly mediated by Ca^{2+} as previously speculated[16,17]. However, several factors indicate that this is a robust interface. The buried surface area is ~1,000 $Å^2$ per protomer (see Supplementary Tables 1&2), similar to that of classical cadherin interfaces (850 $Å^2$ and 1,270 $Å^2$ for type I and type II, respectively). The interface is amphiphilic (Supplementary Fig. 6); all its residues are highly conserved in mouse, human, and chicken homologues and none are predicted to be glycosylated (Fig. 1g and Supplementary Fig. 7). Finally, the same interface was observed in two different crystal lattices, so it is unlikely to represent unphysiological crystal packing interactions.

To further validate the pcdh-15+cdh-23 interface we used isothermal titration calorimetry (ITC) and site-directed mutagenesis. The stoichiometry of the wild-type complex was determined to be $N = 0.88 \pm 0.1$, consistent with the one-to-one crystallographic arrangement (Fig. 1). The measured dissociation constant was $K_D = 2.9 \pm 0.4$ μM ($T = 10°C$, $\Delta H = 7084 \pm 233$ cal/mol, $\Delta S = 50.4 \pm 1.1$ cal/mol/deg, two trials; Fig. 2a,b and Supplementary Discussion). The tip link is thought to be a heterotetramer of parallel protocadherin-15 and cadherin-23 dimers[5] (Fig. 1b). However, our biochemical and crystallographic data do not show homophilic binding of cdh-23 or pcdh-15, suggesting that parallel dimerization is mediated by repeats other than EC1+2. If so, the binding affinity for the heterotetramer is expected to be significantly higher[21].

The "extended handshake" features two main areas of interaction. The first one is located at and above pcdh-15's RXGPP loop and centers on Y8, P19 and I108 in pcdh-15, and L145 and Q187 in cdh-23 (Figs 1g, 2d-f). The second, located between the RXGPP loop and cdh-23's 3_{10} helix, involves I22, R113 and V115 in pcdh-15 along with Y16 and Q98

in cdh-23 (Figs. 1g &2d,g). To test the two interaction areas we introduced mutations predicted to disrupt them: I22A in pcdh-15 (pcdh-15_{I22A}) and L145G in cdh-23 (cdh-23_{L145G}; Fig. 2d,e,g). SEC confirmed proper folding and structural integrity of the mutant proteins. ITC experiments, testing binding with either one or both mutant partners, showed decreased affinity for each single-mutant complex (pcdh-15_{I22A}+cdh-23, K_D > 100 μM; pcdh-15+cdh-23_{L145G}, K_D > 30 μM), and complete lack of interaction for the double-mutant complex (pcdh-15_{I22A}+cdh-23_{L145G}; Fig. 2a,b,d,e,g and Supplementary Figs 2, 8&9). Likewise, SEC of pcdh-15+cadherin-23 EC1 repeats alone did not show complex formation (Supplementary Fig. 2b). Taken together, these results show that the interface observed in the crystals is consistent with the interface observed in solution.

Does the interface have the properties expected for a tip-link bond? Tip links are regularly subjected to (and must withstand) forces ranging from 10 to 100 pN, both *in vivo* and in physiological experiments. While SEC and ITC experiments provide a characterization of the bond in thermodynamic equilibrium, they do not probe its response to mechanical force. To determine whether the pcdh-15+cdh-23 interface is mechanically strong we used steered molecular dynamics (SMD) simulations (Methods and Supplementary Table 3). Force was applied to the C-terminus of each protomer to induce complex dissociation (Fig. 3a). In all SMD simulations of pcdh-15+cdh-23 with Ca^{2+}, unbinding was observed without unfolding of repeats. Partial rupture of the binding interface at contacts formed by residues pcdh-15_{T106} – cdh-23_{L145} and pcdh-15_{R84} – cdh-23_{N96} was followed by sliding of the 3_{10} helix in strand A of cadherin-23 EC1 over the pcdh-15 RXGPP loop, and simultaneous rupture of a salt bridge between pcdh-15_{R113} and cdh-23_{E77} (Fig. 3b and Supplementary Discussion, Figs 10, 11, and Movies I&II). Simulations performed using different stretching speeds, initial conditions, and thermodynamic ensembles revealed a similar scenario with at least one force peak of > 400 pN associated with complex unbinding (Fig. 3c,d and Supplementary Figs 10&11).

Unbinding forces followed the well-known dependence on stretching speed[22], with less force required when the stretch was slower. The slowest speed used in our simulations matched the measured velocity of the basilar membrane induced by loud sound[23] as well

as speeds of mechanical stimulators used in *ex-vivo* electrophysiological experiments[24] (see Supplementary Discussion). In all our simulations the pcdh-15+cdh-23 interface was stronger than that of the classical C-cadherin interface pulled under identical conditions (Supplementary Fig. 12). Furthermore, the predicted force required to unbind parallel complexes was almost double that required to unbind a single pcdh-15+cdh-23 complex (Supplementary Figs 12b,c), which may correspond to the actual force that heterotetrameric tip links can withstand *in vivo* before rupture due to large mechanical stimuli, e.g., loud sound.

The integrity of tip links in hair cells is Ca^{2+}-dependent[3], yet Ca^{2+} does not directly participate in the binding interface. We therefore determined whether the pcdh-15+cdh-23 complex is disrupted by Ca^{2+} removal using SEC experiments in the presence of EGTA (Fig. 4a). The cdh-23 fragment by itself did not show changes in its elution volume, while pcdh-15 in the presence of EGTA showed a shifted elution trace. Importantly, the pcdh-15+cdh-23 complex was disrupted by addition of EGTA: its elution trace did not match that in the presence of Ca^{2+}, but rather corresponded to the summation of the individual components' traces without the shift in elution volume that indicates interaction. The complex used for crystallization is thus Ca^{2+}-dependent at equilibrium, in line with what is known about the full-length protocadherin-15 and cadherin-23 proteins and the tip link[3,5]. To understand the basis of the Ca^{2+} dependence, we performed microsecond-long MD simulations of the Ca^{2+}-free complex. These suggest a molecular mechanism: removal of Ca^{2+} is predicted to cause dissociation indirectly, through entropic stress (see Supplementary Discussion, Supplementary Figs 13 & 14, and Movies III, IV & V), as observed for other cadherins[25].

Over 40 missense mutations associated with deafness in humans or mice target the extracellular domains of protocadherin-15 and cadherin-23. Most modify Ca^{2+}-binding residues[26]. Three human mutations causing inherited deafness (pcdh-15_{D157G}[27], cdh-23_{D101G}[28], and pcdh-15_{R113G}[27]) and one mouse mutation that accelerates progressive hearing loss (cdh-23_{S47P}[29]) are located within the crystallized pcdh-15+cdh-23 complex (Supplementary Figs 1c & 15). Our data provide a structural context to interpret their

effect on tip link function. We also constructed all four mutants to test formation of heterophilic complexes *in vitro* with ITC and SEC, finding that they each affect the pcdh-15+cdh-23 complex in different ways. Cdh-23$_{D101G}$, cdh-23$_{S47P}$, and pcdh-15$_{R113G}$ refolded well as assessed by SEC, whereas pcdh-15$_{D157G}$ did not and its analysis was not possible. The D101G and S47P cdh-23 fragments crystallized in complex with pcdh-15 and show only minor changes in the interface and in binding (Fig. 2c, Supplementary Discussion and Supplementary Fig. 16). On the other hand, pcdh-15$_{R113G}$ showed impaired binding to cdh-23.

Residue pcdh-15$_{R113}$ is of particular interest because it is at the interface between pcdh-15 and cdh-23 (Fig. 2h). Mutation R113G, causing human non-syndromic deafness DFNB23[27], eliminates the long arginine sidechain that flanks the hydrophobic core of this interface and disrupts its integrated hydrogen-bond network. SEC of either co-refolded or independently refolded proteins showed no evidence of pcdh-15$_{R113G}$+cdh-23 complex formation (Fig. 4b and Supplementary Fig. 2). Furthermore, ITC experiments show impaired binding and indicate an estimated K_D at least an order of magnitude larger than that measured for wild-type pcdh-15+cdh-23 (>20 μM, Fig. 2c and Supplementary Fig. 8). In other work, R113G impaired binding of full-length protocadherin-15 and cadherin-23 *in vitro*[5], as well as binding of protein fragments to hair-cell tip links *ex vivo*[11]. Together, these observations help validate the interface observed in our crystal structure and indicate that this mutation causes deafness by directly interfering with binding between cadherin-23 and protocadherin-15. Residual interactions detected in ITC experiments may explain why vestibular function is not affected in human subjects carrying this mutation[27].

In summary (Supplementary Fig. 1), the pcdh-15+cdh-23 structure provides the first view of a heterophilic cadherin complex, revealing a novel “extended handshake” interface that simulations predict to be mechanically stronger than required to resist forces produced by moderate sound. The structure helps explain the Ca^{2+} sensitivity of the tip link, and the etiology of certain inherited deafnesses. For other cadherins, both the existence of heterophilic cadherin bonds and the possibility of interdigitation have been

debated[20]. While protocadherin-15 and cadherin-23 are rather specialized members of the cadherin family, the overlapping heterophilic complex formed by these molecules suggests structural determinants that could also favor this type of interactions in related members of the cadherin family, such as the fat3 and fat4 cadherins that control neuronal morphology and morphogenesis[30] (Supplementary Discussion).

Methods Summary

Wild-type and mutant mouse cadherin-23 repeats EC1+2 and protocadherin-15 EC1+2 were subcloned into pET21a, expressed independently in BL21CodonPlus(DE3)-RIPL, purified under denaturing conditions with Ni-sepharose beads, and then mixed and co-refolded in six steps at 4°C. Refolded proteins were further purified by SEC. Crystals were grown by vapor diffusion, cryoprotected, and cryo-cooled in N_2. X-ray diffraction data were collected as indicated in Supplementary Tables 1&2. Structures were determined by molecular replacement. ITC experiments were carried out using a MicroCal ITC_{200} calorimeter with buffer-matched samples at 10°C. Analytical SEC was performed on a Superdex200 PC3.2/3.0 column on an AKTAmicro. Systems for MD simulations were prepared with VMD. MD simulations were performed using NAMD 2.7 or Anton with the CHARMM27 force field, the CMAP correction, and the TIP3P water model. Interfaces of complexes were analyzed with VMD and the PISA server.

References

1. Gillespie, P. G. and Müller, U. Mechanotransduction by hair cells: Models, molecules, and mechanisms. *Cell* **139**, 33–44 (2009).

2. Pickles, J. O., Comis, S. D., and Osborne, M. P. Cross-links between stereocilia in the guinea pig organ of corti, and their possible relation to sensory transduction. Hear. Res. 15, 103–112 (1984).

3. Assad, J. A., Shepherd, G., and Corey, D. P. Tip-link integrity and mechanical transduction in vertebrate hair cells. *Neuron* **7**, 985–994 (1991).

4. Ahmed, Z. M., et al. The tip-link antigen, a protein associated with the transduction complex of sensory hair cells, is protocadherin-15. *J. of Neurosci.* **26**, 7022–7034 (2006).

5. Kazmierczak, P., et al. Cadherin 23 and protocadherin 15 interact to form tip-link filaments in sensory hair cells. *Nature* **449**, 87–91 (2007).

6. Alagramam, K. N., et al. The mouse Ames waltzer hearing-loss mutant is caused by mutation of Pcdh15, a novel protocadherin gene. *Nat. Genet.* **27**, 99–102 (2001).

7. Ahmed, Z. M., et al. Mutations of the protocadherin gene PCDH15 cause Usher syndrome type 1F. *Am. J. Hum. Genet.* **69,** 25-34 (2001).

8. Bolz, H. et al. Mutation of CDH23, encoding a new member of the cadherin gene family, causes Usher syndrome type 1D. *Nat. Genet.* **27**, 108-112 (2001)

9. Bork, J. M., et al. Usher syndrome 1D and nonsyndromic autosomal recessive deafness DFNB12 are caused by allelic mutations of the novel cadherin-like gene CDH23. *Am. J. Hum. Genet.* **68**, 26-27 (2001).

10. Di Palma, et al. Mutations in Cdh23, encoding a new type of cadherin, cause stereocilia disorganization in waltzer, the mouse model for Usher syndrome type 1D. *Nat. Genet.* **27**, 103–107 (2001).

11. Lelli, A., Kazmierczak, P., Kawashima, Y., Muller, U., and Holt, J. R. Development and regeneration of sensory transduction in auditory hair cells requires functional interaction between cadherin-23 and protocadherin-15. *J. Neurosci.* **30**, 11259–11269 (2010).

12. Takeichi, M. Cadherin cell adhesion receptors as a morphogenetic regulator. *Science* **251**, 1451–1455 (1991).

13. Gumbiner, B. M. Regulation of cadherin-mediated adhesion in morphogenesis. *Nat. Rev. Mol. Cell Biol.* **6**, 622–634 (2005).

14. Shapiro, L., Love, J., and Colman, D. R. Adhesion molecules in the nervous system: structural insights into function and diversity. *Annu. Rev. Neurosci.* **30**, 451–474 (2007).

15. Rouget-Quermalet, et al. Protocadherin 15 (PCDH15): a new secreted isoform and potential marker for NK/T cell lymphomas. *Oncogene* **25**, 2807–2811 (2006).

16. Sotomayor, M., Weihofen, W. A., Gaudet, R. G., and Corey, D. P. Structural determinants of cadherin-23 function in hearing and deafness. *Neuron* **66**, 85–100 (2010).

17. Elledge, H. M., et al. Structure of te N terminus of cadherin 23 reveals a new adhesion mechanism for a subset of cadherin superfamily members. *Proc. Natl. Acad. Sci. USA* **107**, 10708–100712 (2010).

18. Hulpiau, P. and van Roy, F. Molecular evolution of the cadherin superfamily. *The International Journal of Biochemistry and Cell Biology* **41**, 349–369 (2009).

19. Brasch, J., Harrison, O. J., Honig, B., and Shapiro, L. Thinking outside the cell: how cadherins drive adhesion. *Trends Cell Biol.* **22**, 299-310 (2012).

20. Leckband, D. and Prakasam, A. Mechanism and dynamics of cadherin adhesion. *Annu. Rev. Biomed. Eng.* **8**, 259–287 (2006).

21. Kuriyan, J. and Eisenberg, D. The origin of protein interactions and allostery in colocalization. *Nature*, **450**, 983-990 (2007).

22. Evans, E. and Ritchie, K. Dynamic strength of molecular adhesion bonds. *Biophys. J.* **72**, 1541-1555 (1997).

23. Robles, L. and Ruggero, M. A. Mechanics of Mammalian Cochlea. *Physiological Reviews,* **81**, 1305-1352 (2001).

24. Stauffer, E. A. and Holt, J. R. Sensory Transduction and Adaptation in Inner and Outer Hair Cells of the Mouse Auditory System. *J. Neurophysiol.* **98**, 3360-3369 (2007).

25. Häussinger, D., et al. Calcium-dependent homoassociation of E-cadherin by NMR-spectroscopy: changes in mobility, conformation and mapping of contact regions. *J. Mol. Biol.* **324**, 823-839 (2002).

26. de Brouwer, A. P. M. et al. Mutations in the calcium-binding motifs of cdh23 and the 35delg mutation in gjb2 cause hearing loss in one family. *Hum. Genet.* **112**, 156–163 (2003).

27. Ahmed, Z. M., et al. Gene structure and mutant alleles of PCDH15: nonsyndromic deafness DFNB23 and type 1 Usher syndrome. *Hum. Genet.* **124**, 215–223 (2008).

28. Astuto, L. M., et al. CDH23 mutation and phenotype heterogeneity: a profile of 107 diverse families with usher syndrome and nonsyndromic deafness. *Am. J. Hum. Genet.* **71**, 262–275 (2002).

29. Han, F., et al. A new mouse mutant of the Cdh23 gene with early-onset hearing loss facilitates evaluation of otoprotection drugs. *Pharmacogenomics J.* **12**, 30–44 (2012).

30. Deans, M. R. et al. Control of neuronal morphology by the atypical cadherin fat3. *Neuron*, **71**, 820–832 (2011).

Supplementary Information

Supplementary Information is linked to the online version of the paper at www.nature.com/nature.

Acknowledgements

We thank Bruce Derfler for assistance with mutagenesis, Dr. Victoria D'Souza and her laboratory for advice on calorimetry, and the Corey and Gaudet laboratories for helpful discussions. Full-length cDNAs of cdh23 and pcdh15 used as template for some of our constructs were kindly provided by Dr. U. Müller (TSRI) and Dr. T. B. Friedman (NIH). This work was supported by NIH (R01 DC02281 to D.P.C.; RC2GM093307 to NRBSC/PSC) and NSF through TeraGrid/XSEDE (TRAC MCB080015). Simulations were performed at the NCSA-Abe, NICS-Kraken, TACC-Ranger, and PSC-Anton supercomputers. Use of APS beamlines was supported by NIH award RR-15301 and DOE contract No. DE-AC02-06CH11357. Use of ALS beamline 4.2.2 was supported by DOE contract No. DE-AC02-05CH11231. M.S. was a HHMI Fellow of the Helen Hay Whitney Foundation and D.P.C. is an HHMI Investigator.

Author Contributions

All authors participated in all parts of this study. MS did all experiments and simulations.

Author Information

Atomic coordinates and structure factors for the reported crystals structures have been deposited with the Protein Data Bank under accession codes 4apx (S1a), 4axw (S1b), 4aq8 (S2), 4aqa (S3), and 4aqe (S4). Reprints and permissions information is available at www.nature.com/reprints. The authors declare no competing financial interests. Correspondence and requests for materials should be addressed to D.P.C. (dcorey@hms.harvard.edu) or R.G. (gaudet@mcb.harvard.edu).

Legends to Figures

Figure 1. Structure of tip-link protocadherin-15 bound to cadherin-23. **a**, Hair-cell stereocilia bundle. A tip-link filament extends from the tip of each stereocilium to the side of its tallest neighbour. **b**, The tip link formed by a protocadherin-15 parallel dimer interacting tip-to-tip with a cadherin-23 parallel dimer[5]. These proteins feature 11 and 27 extracellular cadherin (EC) repeats, respectively. Inset shows possible arrangement at the junction. **c**, Ribbon diagram of protocadherin-15 EC1+2 (pcdh-15; purple) bound to cadherin-23 EC1+2 (cdh-23; blue) with Ca^{2+} ions as green spheres. Arrowheads indicate pcdh-15's RGGPP loop and cdh-23's 3_{10} helix. Residues R113, C11, and C99 of pcdh-15 are shown in stick representation. **d**, Detail of disulfide bond C11-C99 and isoform-dependent residues D4-Y8 at the pcdh-15 N-terminus. **e**, Detail of Ca^{2+}-binding sites 1, 2, and 3 at the pcdh-15 linker. Protein backbone and sidechains are in cartoon and stick representations, respectively. **f**, Surface representation of pcdh-15 (purple and pink) and cdh-23 (blue and cyan) as in (c). **g**, Pcdh-15 and cdh-23 interaction surfaces exposed with interfacing residues labeled.

Figure 2. Pcdh-15+cdh-23 complex formation probed using isothermal titration calorimetry (ITC) and site-directed mutagenesis. **a**, Raw power vs. time data for pcdh-15 (111 μM) titrated with cdh-23 (1.1 mM) at 10°C (black, WT-WT). Inset shows raw data (blue) for pcdh-15_{I22A} (114 μM) titrated with cdh-23_{L145G} (1.2 mM). **b-c**, Change in molar enthalpy for pcdh-15 titrated with cdh-23 (black); pcdh-15_{I22A} with cdh-23 (light green); pcdh-15 with cdh-23_{L145G} (dark green); pcdh-15_{I22A} with cdh-23_{L145G} (blue); pcdh-15 with cdh-23_{S47P} (violet); pcdh-15_{R113G} with cdh-23 (magenta); and pcdh-15 with cdh-23_{D101G} (indigo; concentrations in Supplementary Fig. 8). Sigmoidal isothermals were observed only for pcdh-15+cdh-23 and pcdh-15+cdh-23_{S47P}. **d-h**, Details of pcdh-15+cdh-23 interface, highlighting residue L145 (e), the RXGPP loop (f), and residues I22 (g) and R113 (h). Panel (h) is a 180°-rotated version of panel (g). Protein backbone and interfacing residues (as identified by PISA) are in purple/pink for pcdh-15 and blue/cyan for cdh-23.

Figure 3. Mechanical strength of the pcdh-15+cdh-23 complex probed by steered molecular dynamics (SMD) simulations. **a**, Snapshots of pcdh-15 (purple) and cdh-23 (blue) unbinding during simulation SNA7 (Supplementary Table 3). The complex is shown in both cartoon and surface representations at the beginning, and in surface representation at indicated time points. Force was applied to the C-termini of both protomers (Supplementary Movies I&II). Green arrows point to broken interfaces. **b**, Region of gray box in panel (a), showing interacting residues during unbinding. **c**, Force applied to one C-terminus versus distance between C-termini ends of pcdh-15 and cdh-23. Different traces correspond to independent simulations performed at stretching speeds of 10 (blue and black), 1 (light and dark green), 0.1 (cyan, 1-ns running average shown in black), and 0.02 nm/ns (magenta, 1-ns running average). Snapshots in (a) are indicated by arrowheads. **d**, Maximum force-peak values vs. stretching speed for unbinding simulations of pcdh-15+cdh-23 started after a 1-ns or 1-μs equilibration (light green, SN2 to SN6; dark green, SNA2 to SNA7; cyan, SN10 to SN13). Simulations SN2-SN6 and

SNA2-SNA7 used the S1b structure and SN10-SN13 used S1a; unbinding forces for all three sets were equivalent.

Figure 4. Pcdh-15+cdh-23 complex formation, its Ca^{2+}-dependence, and the role of the deafness mutation R113G, probed using analytical size exclusion chromatography (SEC). Individual traces represent independent experiments. **a**, **top**, SEC traces for pcdh-15 and cdh-23 with Ca^{2+} (red and blue) or with 5 mM EGTA (purple and cyan). A shift upon Ca^{2+} removal by EGTA was observed for pcdh-15 (purple vs. red curves). **middle**, SEC traces for pcdh-15+cdh-23 in the presence of Ca^{2+} (light green) or 5 mM EGTA (dark green). The summation of a purple and a cyan curve from above is shown as a dashed line. The EGTA-treated complex behaved as the sum of its EGTA-treated components, indicating Ca^{2+}-dependent complex formation. **bottom**, Coomassie-stained SDS-PAGE of eluted fractions from EGTA-treated proteins. **b**, **top**, SEC traces for mutant pcdh-15_{R113G} alone (maroon), and mixed with cdh-23 (orange). Wild-type proteins from (a) are shown for comparison. **bottom**, Coomassie-stained SDS-PAGE of eluted fractions aligned to chromatogram. A reproducible shift in elution volume was observed for the wild-type (green) but not for the mutant mixture (pcdh-15_{R113G}+cdh-23; orange). The shifted peak (1.61 ml) contained both proteins (1.56 to 1.64 ml fractions).

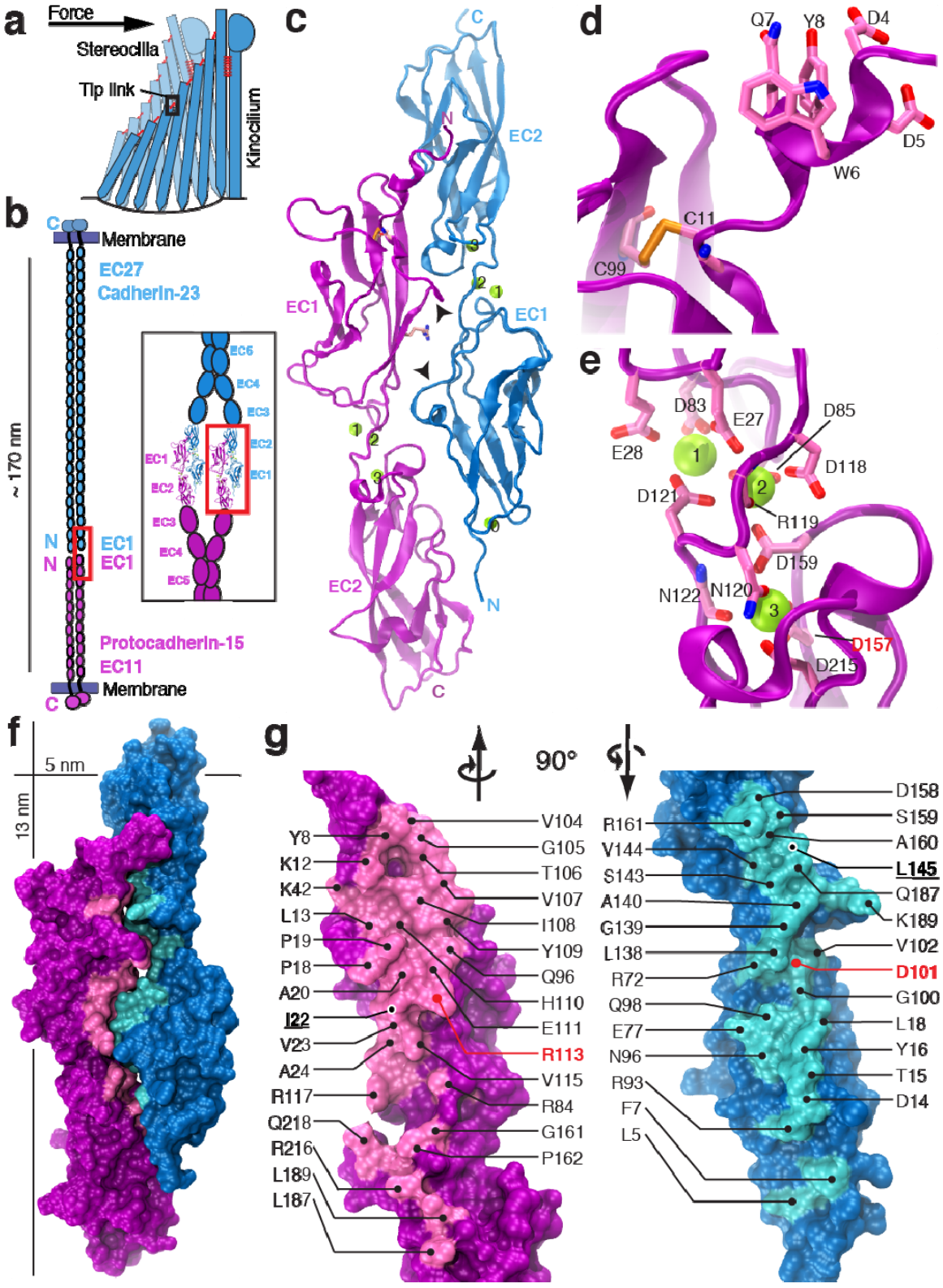
a
Force
Stereocilia
Tip link
Kinocilium
b
C
Membrane
EC27
Cadherin-23
~ 170 nm
N
N
EC1
EC1
EC6
EC4
EC3
EC2
EC1
EC1
EC2
EC3
EC4
EC5
Protocadherin-15
EC11
Membrane
C
c
C
N
EC2
EC1
EC1
EC2
N
C
d
Q7
Y8
D4
D5
W6
C11
C99
e
D83
E27
D85
E28
D118
D121
R119
D159
N122
N120
D157
D215
f
5 nm
13 nm
g
90°
V104
G105
T106
V107
I108
Y109
Q96
H110
E111
R113
V115
R84
G161
P162
Y8
K12
K42
L13
P19
P18
A20
I22
V23
A24
R117
Q218
R216
L189
L187
D158
S159
A160
L145
Q187
K189
V102
D101
G100
L18
Y16
T15
D14
R161
V144
S143
A140
G139
L138
R72
Q98
E77
N96
R93
F7
L5

Figure 1

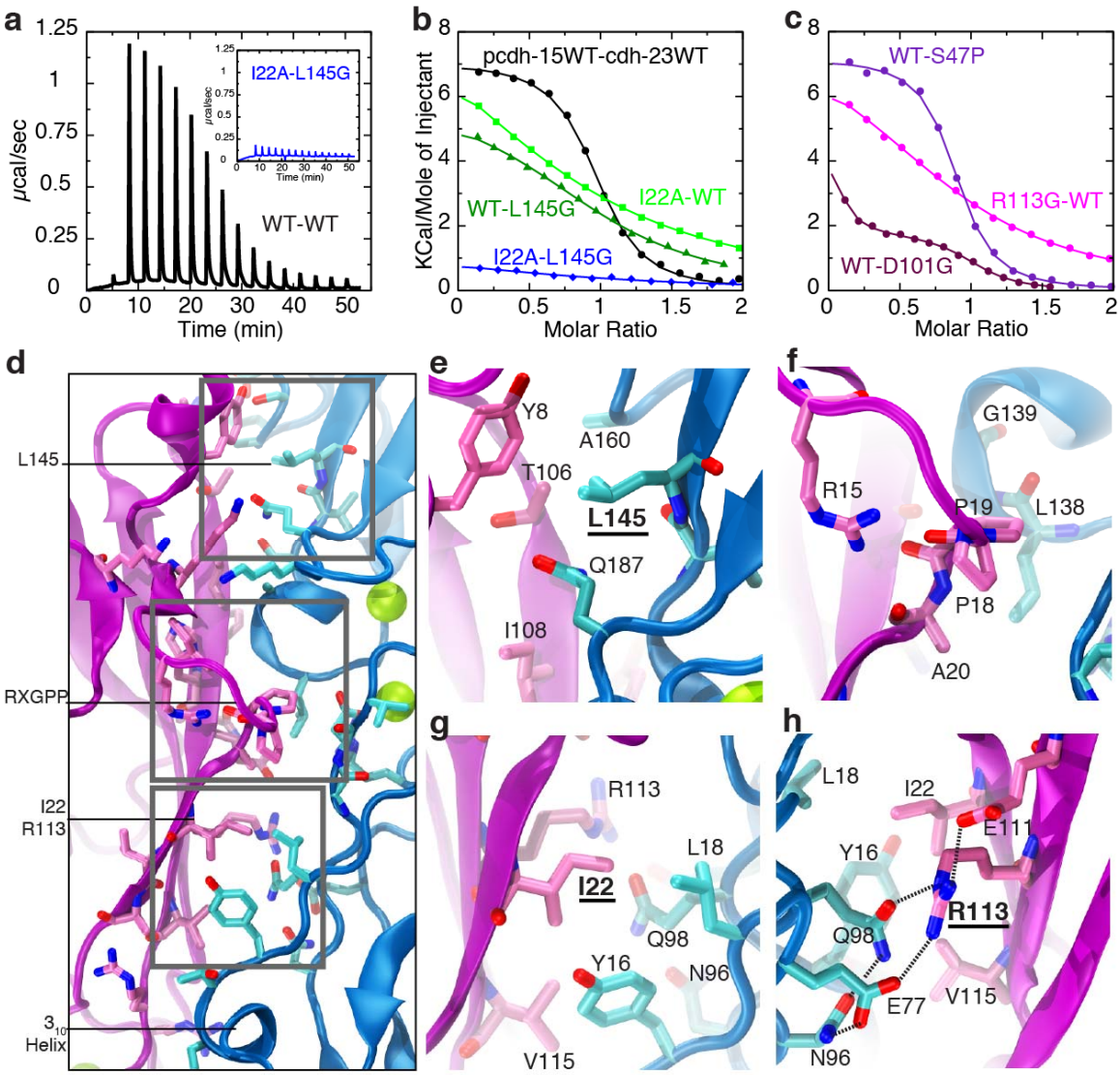
a
μcal/sec
Time (min)
WT-WT
I22A-L145G
b
KCal/Mole of Injectant
Molar Ratio
pcdh-15WT-cdh-23WT
WT-L145G
I22A-WT
I22A-L145G
c
Molar Ratio
WT-S47P
R113G-WT
WT-D101G
d
L145
RXGPP
I22
R113
3₁₀ Helix
e
Y8
A160
T106
L145
Q187
I108
f
G139
R15
P19
L138
P18
A20
g
R113
L18
I22
Q98
Y16
N96
V115
h
L18
I22
E111
Y16
R113
Q98
E77
V115
N96

Figure 2

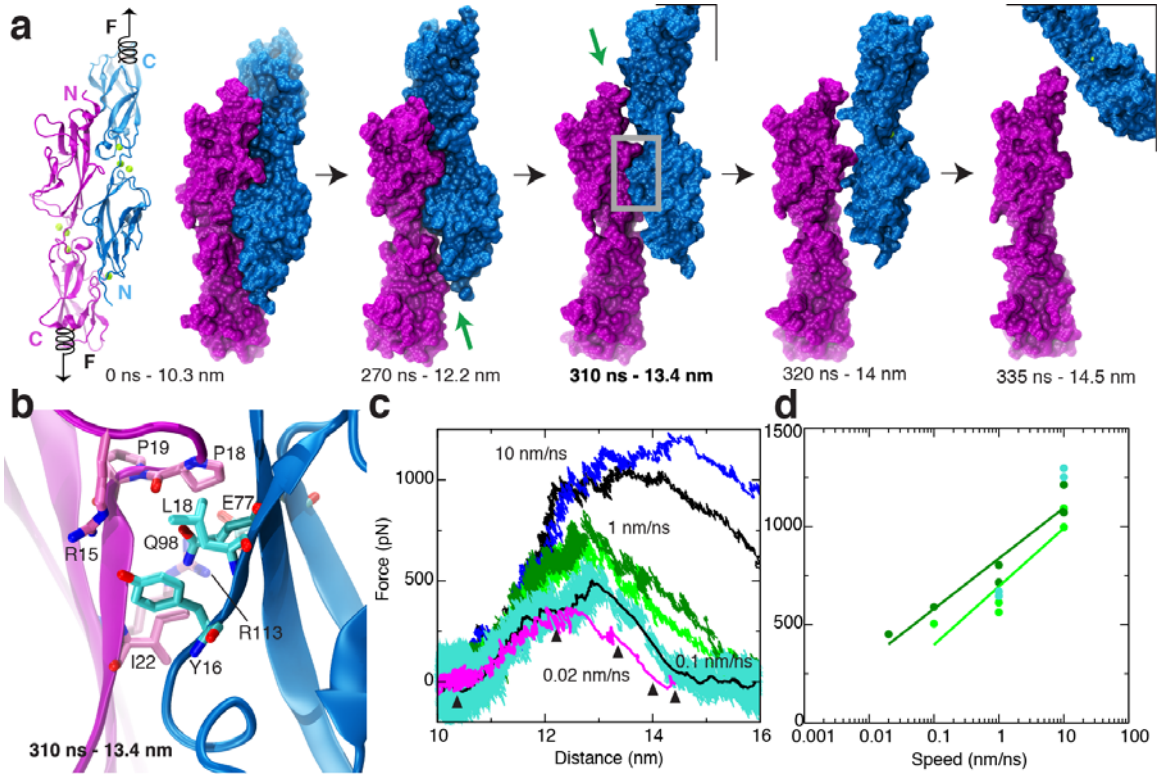
a
F
C
N
N
C
F
0 ns - 10.3 nm
270 ns - 12.2 nm
310 ns - 13.4 nm
320 ns - 14 nm
335 ns - 14.5 nm
b
P19
P18
L18
E77
Q98
R15
R113
I22
Y16
310 ns - 13.4 nm
c
10 nm/ns
1 nm/ns
0.1 nm/ns
0.02 nm/ns
Force (pN)
Distance (nm)
d
Speed (nm/ns)

Figure 3

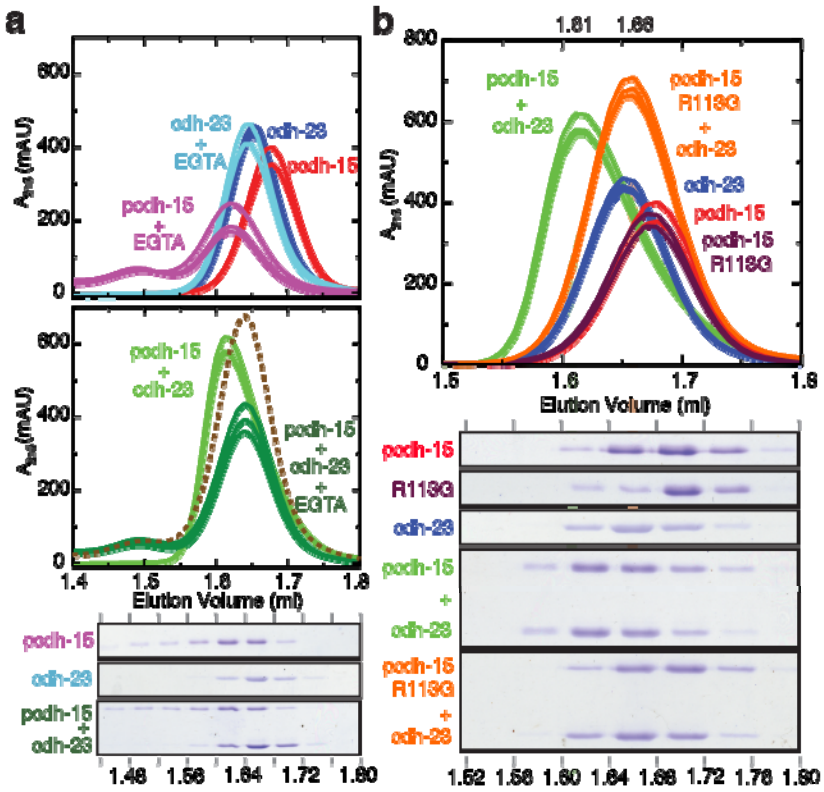
a
b
cdh-23
+
EGTA
cdh-23
pcdh-15
pcdh-15
+
EGTA
pcdh-15
+
cdh-23
pcdh-15
+
cdh-23
+
EGTA
Elution Volume (ml)
pcdh-15
cdh-23
pcdh-15
+
cdh-23
pcdh-15
+
cdh-23
pcdh-15
R113G
+
cdh-23
cdh-23
pcdh-15
pcdh-15
R113G
Elution Volume (ml)
pcdh-15
R113G
cdh-23
pcdh-15
+
cdh-23
pcdh-15
R113G
+
cdh-23

Figure 4

Online Methods

Cloning, expression, and purification of protocadherin-15 and cadherin-23 repeats

Clones of mouse cadherin-23 repeats EC1 and EC1+2 were previously described[16]. Numbering corresponds to mouse cadherin-23 and protocadherin-15 without their signal sequences. Mouse protocadherin-15 EC1+2 comprising residues Q1 to D233 (Q27 to D259 in NP_001136218.1) was subcloned into the NdeI and XhoI sites of the vector pET21a (C-terminal His-tag). The signal sequence was replaced by a methionine at position 0. The R113G, D157G, and I22A mutations in pcdh-15, as well as the L145G and S47P mutations in cdh-23 were generated using the QuikChange Lightning mutagenesis kit (Stratagene). All constructs were verified by DNA sequencing. Pcdh-15, pcdh-15$_{R113G}$, pcdh-15$_{D157G}$, pcdh-15$_{I22A}$, cdh-23, cdh-23$_{D101G}$, cdh-23$_{S47P}$, and cadherin-23 EC1 were expressed independently in BL21CodonPlus(DE3)-RIPL (Stratagene) cultured in LB and induced at OD_{600}=0.6 with 100 µM IPTG at room temperature for ~16 hrs. Cells were lysed by sonication in denaturing buffer (20 mM HEPES at pH 7.5, 6 M guanidine hydrochloride [GuHCl], 10 mM $CaCl_2$, 20 mM imidazole at pH 7.0). The cleared lysates were loaded onto Ni-sepharose (GE Healthcare) and eluted with denaturing buffer supplemented with 500 mM imidazole. Wild-type and mutant Pcdh-15 protein fragments were reduced by adding 1 mM DTT and incubating at 37°C for ~30 min. Purified and denatured samples were mixed (pcdh-15+cdh-23, pcdh-15$_{R113G}$+cdh-23, pcdh-15$_{D157G}$+cdh-23, pcdh-15+cdh-23$_{D101G}$, pcdh-15+cdh-23$_{S47P}$, pcdh-15+cadherin-23 EC1, pcdh-15$_{R113G}$+cadherin-23 EC1, and pcdh-15$_{I22A}$+cadherin-23 EC1) and co-refolded in six steps at 4°C using MWCO 2000 membranes (protocol adapted from ref 31). First, the mixture was dialyzed for 24 hrs against D buffer (20 mM Tris HCl pH 8.0, 10 mM $CaCl_2$) with 6 M GuHCl, followed by two 24-hr dialyses against D buffer with 3 and 2 M GuHCl, respectively. The last three steps consisted of 12-hr dialyses against D buffer with decreasing GuHCl concentration (1, 0.5, and 0 M) plus 400 mM L-Arg and 375 µM GSSG. Refolded protein used for crystallization was further purified in two consecutive size-exclusion chromatography (SEC) experiments with relevant fractions on a Superdex75 column (GE Healthcare) in 20 mM TrisHCl pH 8.0, 200 mM KCl, with 10 and 1 mM $CaCl_2$, respectively. Predicted and apparent molecular weights (SDS-PAGE) for pcdh-15 and cdh-23 fragments were 27.5/37 kDa and 23.8/25 kDa, respectively. Identity of pcdh-15 was confirmed through N-terminal sequencing.

Crystallization, data collection, and structure determination

Crystals were grown by vapor diffusion at 4°C by mixing equal volumes of protein (5-10 mg/ml) and reservoir solution of (0.1 M MES pH 6.5, 8% w/v PEG 8000) for S1a, (0.1 M MES pH 6.5, 15% w/v PEG 550 MME) for S1b, (0.1 M HEPES pH 7.5, 10% w/v PEG 8000) for S2, (0.1M MES pH 6.5, 8% w/v PEG 20000) for S3, and (0.1M MES pH 6.5, 12% PEG 4000) for S4. All crystals were cryoprotected in reservoir solution plus 25% glycerol and cryo-cooled in N_2. X-ray diffraction data were collected as indicated in Supplementary Tables 1&2 and processed with HKL2000[32]. Structures were determined by molecular replacement using the cdh-23 structure (pdb code 2wcp) and a pcdh-15 homology model (based on the same cdh-23 structure) as search models with Phaser[33]. Model building was done using COOT[34] and restrained TLS refinement using REFMAC5[35]. The final models include residues M0 to E207 (cdh-23) and M0 to H237

(pcdh-15) for S1a, M0 to E207 (cdh-23) and Q1 to H236 (pcdh-15) for S1b, M0 to E207 (cdh-23 A and B) and Q1/Y2 to H237 (pcdh-15 C and D) for S2, M0 to D205 (cdh-23_{D101G} and cdh-23_{S47P}) and M0 to H236/H237 (pcdh-15) for S3 and S4. Data collection and refinement statistics are provided in Supplementary Tables 1&2. Coordinates have been deposited in the Protein Data Bank with entry codes 4apx (S1a), 4axw (S1b), 4aq8 (S2), 4aqa (S3), and 4aqe (S4).

Isothermal titration calorimetry

ITC experiments were carried out using a MicroCal ITC_{200} calorimeter and designed following guidelines from Thomson and Ladbury[36] and the manufacturer's manual. Wild type, I22A and R113G pcdh-15 fragments were co-refolded with cadherin-23 EC1 as described above, and subsequent SEC was performed on a Superdex75 column with 20 mM TrisHCl pH 8.0, 300 mM NaCl, and 1 mM $CaCl_2$. Fractions with pure pcdh-15, pcdh-15_{I22A}, and pcdh-15_{R113G} were collected, concentrated (to 100 to 150 μM) and placed in the calorimeter's sample cell. Similarly, wild type, L145G, D101G, and S47P cdh-23 fragments were refolded as previously described[16], concentrated (to 1 to 2 mM), buffer-matched through SEC, and then used as titrants. Protein concentrations were measured using samples' absorbances at 280 nm and theoretical extinction coefficients. All experiments were performed at 10°C, as no signal was detected and the protein tended to be unstable at room temperature. In a typical experiment, an initial 0.5-μl injection (disregarded in analyses) was followed by fifteen 2.44-μl injections of titrant (Δt = 3 min). Experiments and controls with each combination of fragments were repeated at least once (Supplementary Fig. 8). Fittings and binding constants were obtained using the MicroCal Software, a model with one set of sites, and blank-subtracted data. Fitting parameters are reported for saturating sigmoidal curves as the average±s.d. of two independent experiments. Attempts to obtain saturating sigmoidal curves and precise K_Ds for mutant proteins were hampered by aggregation of protein samples at the high concentration required (>2 mM).

Analytical size exclusion chromatography

SEC of co-refolded proteins (pcdh-15+cdh-23, pcdh-15_{R113G}+cdh-23, pcdh-15_{D157G}+cdh-23, pcdh-15+cdh-23_{D101G}, pcdh-15+cdh-23_{S47P}, pcdh-15+cadherin-23 EC1, and pcdh-15_{R113G}+cadherin-23 EC1) was performed on a Superdex75 16/60 column with 20 mM TrisHCl pH 8.0, 300 mM NaCl and 1 mM $CaCl_2$ (Supplementary Fig. 2). Fractions with pure cdh-23 (excess from pcdh-15+cdh-23), pcdh-15 (from pcdh-15+cadherin-23 EC1), and pcdh-15_{R113G} (from pcdh-15_{R113G}+cadherin-23 EC1) were collected, concentrated (~0.5 mg/ml), and used for subsequent analytical SEC (Fig 4a,b) on a Superdex200 PC3.2/3.0 column equilibrated with the same buffer (plus 5 mM EGTA when indicated). Experiments were performed at 4°C using a 10 μl loop and a 50 μl/min flow rate on an AKTAmicro system equipped with a fused silica capillary tubing for collection of 40 μl fractions. EGTA was added to individual or pre-mixed concentrated samples followed by a 1 hr mild shaking prior to SEC.

Simulated systems

The psfgen, solvate, and autoionize VMD[37] plug-ins were used to build all systems (Supplementary Table 3) as previously reported[16]. Most of the pcdh-15+cdh-23 complex

simulations used structure S1b (which we determined first) except simulations SN9 to SN13 (which used higher resolution structure S1a; Supplementary Tables 1 and 3). Structures with non-native N- and C-terminal tails were modified back to native sequences. Systems without bound Ca^{2+} were prepared by replacing Ca^{2+} atoms with K^{+}.

Molecular dynamics simulations using NAMD

MD simulations were performed using NAMD 2.7[38], the CHARMM27 force field for proteins with CMAP correction[39,40], and the TIP3P model for water. Simulation parameters were as in ref 16, except for simulations SNA7 and SNC6, in which a multiple-time-step scheme was used with electrostatic interactions evaluated every other time step. Parameters for Ca^{2+} were from ref 41. Each system was energy-minimized, then equilibrated in the constant number, pressure, and temperature ensemble (NpT), and the resulting state used to perform subsequent Anton or SMD simulations[42]. All simulations used T=310 K. Coordinates of all atoms were saved for analysis every picosecond. Constant velocity stretching simulations used the SMD method and NAMD Tcl Forces interface[16,43].

Molecular dynamics simulations using Anton

Anton is a massively parallel special-purpose machine for molecular dynamics simulations[44]. Systems pre-equilibrated in NAMD (1.1 ns, T=310 K) were converted to the Anton-compatible Maestro format using the convertNAMDtoMaestro.py script provided by NRBSC/PSC. Anton and NAMD simulations used the same force field. Hydrogen atoms were constrained with SHAKE. Restraints were applied to C_α atoms of residues 121, 173, and 205 of cdh-23 to avoid rotation of the complex and contact between periodic images. A multiple-time-step scheme was used with interactions evaluated every 2.5 fs, except for non-bonded interactions computed every other time step. A set of cutoff radii and parameters for evaluation of electrostatic forces was automatically generated for each simulated system using the guess_anton_config script. Simulations were performed in either the constant number, volume, and temperature ensemble (NVT) using the Nose-Hoover thermostat, or the constant number, pressure, and temperature ensemble (NpT) using the Berendsen thermostat/barostat. Center of mass motion was removed. Coordinates of all atoms were saved for analysis every 50 (NpT) or 200 (NVT) picoseconds. Anton simulations are restricted in size (<120,000 atoms) and cannot incorporate SMD-like forces, hence the use of complementary NAMD simulations.

Analysis tools

The Protein Interfaces, Surfaces and Assemblies (PISA) server was used to analyze complex interfaces[45] and identify residues shown in Figs 1g and 2d. The VMD “measure SASA” command was used to determine interface area throughout simulations with a probe radius of 1.4 Å. Interface area was defined as the difference in total solvent-accessible surface areas for each isolated protomer and for the complex divided by two. Glycosylation sites were predicted using OGPET[46], NetNGlyc[47] and NetOGlyc[48]. Intradomain RMSD and interdomain flexing were analyzed using DynDom[49]. Regression fits to data points of maximum force peaks versus stretching speeds were performed using a logarithmic expression of the form $y = a + b \log x$. Plots and curve fits were

prepared using xmgrace. Molecular images in this paper were created with the molecular graphics program VMD[37], except for Supplementary Fig. 5 which used PyMOL (Schrödinger, LLC).

Methods references

31. Tsumoto, K. et al. Highly efficient recovery of functional single-chain Fv fragments from inclusion bodies overexpressed in Escherichia coli by controlled introduction of oxidizing reagent–application to a human single-chain Fv fragment. *J. Immmuno. Meth.* **219**, 119-129 (1998).

32. Otwinowski, Z. and Minor, W. Processing of x-ray diffraction data collected in oscillation mode. *Methods Enzymol.* **276**, 307-326 (1997).

33. McCoy, A. J. et al. Phaser crystallographic software. *J. Appl. Cryst.* **40**, 658-674 (2007).

34. Emsley, P and Cowtan, K. Coot: Model-building tools for molecular graphics. *Acta Crystallogr. D Biol. Crystallogr.* **60**, 2126-2132 (2004).

35. Murshudov, G. N., Vagin, A. A. and Dodson, E. J. Refinement of macromolecular structures by the maximum-likelihood method. *Acta Crystallogr. D Biol. Crystallogr.* **53**, 240-255 (1997).

36. Thomson, J. A. and Ladbury, J. E. Isothermal Titration Calorimetry: a Tutorial. In *Biocalorimetry 2: Applications of Calorimetry in the Biological Sciences* edited by John E. Ladbury and Michael L. Doyle. John Wiley & Sons Ltd., 37-58 (2004).

37. Humphrey, W., Dalke, A., and Schulten, K. VMD – Visual Molecular Dynamics. *J. Mol. Graphics* **14**, 33-38 (1996).

38. Phillips, J. C. et al. Scalable molecular dynamics with NAMD. *J. Comp. Chem.* **26**, 1781-1802 (2005).

39. MacKerell, Jr. A., et al. All-atom empirical potential for molecular modeling and dynamics studies of proteins. *J. Phys. Chem. B* **102**, 3586-3616 (1998).

40. MacKerell, Jr. A. D., Feig, M. and Brooks III, C. L. Extending the treatment of backbone energetics in protein force fields: Limitations of gas-phase quantum mechanics in reproducing protein conformational distributions in molecular dynamics simulations. *J. Comp. Chem.* **25**, 1400-1415 (2004).

41. Marchand, S. and Roux, B. Molecular dynamics study of calbindin d9k in the apo and singly and doubly calcium-loaded states.*Proteins: Struct., Func., Gen.* **33**, 265-284 (1998).

42. Sotomayor, M. and Schulten, K. Single-molecule experiments in vitro and in silico. Science 316, 1144–1148 (2007).

43. Sotomayor, M. and Schulten, K. The allosteric role of the Ca^{++} switch in adhesion and elasticity of C-cadherin. *Biophys. J.* **94**, 4621–4633 (2008).

44. Shaw, D. E., et al. Atomic-level characterization of the structural dynamics of proteins. *Science* **330**, 341–346 (2010).

45. Krissinel, E. and Henrick, K. Inference of macromolecular assemblies from crystalline state. *J. Mol. Biol.* **372**, 774-799 (2007).

46. http://ogpet.utep.edu/OGPET/

47. http://www.cbs.dtu.dk/services/NetNGlyc/

48. http://www.cbs.dtu.dk/services/NetOGlyc/

49. Hayward, S. and Berendsen, H. J. Systematic analysis of domain motions in proteins from conformational change: new results on citrate synthase and T4 lyzozyme *Proteins,* **30**, 144-154 (1998).

Supplementary Information

Structure of a Force-Conveying Cadherin Bond Essential for Inner-Ear Mechanotransduction

Marcos Sotomayor, Wilhelm A. Weihofen, Rachelle Gaudet, David P. Corey

Supplementary Discussion

Cadherin dissociation constants

Reported K_D values for classical cadherins[50-52] have been measured using analytical ultracentrifugation and range from ~1 to ~100 μM at 25°C. Measurements for type II cadherins indicate K_D values in the lower μM range, while values for type I cadherins are usually >20 μM. For instance, a type II VE-cadherin construct with 5 EC repeats has a K_D of 1 μM at 25°C[52], while K_D values for type I N-cadherin EC1+2 are ~26 μM at 25°C[51]. Interestingly, some classical cadherin K_D values are temperature dependent (values for type I E-cadherin EC1+2 at 25°C and 37°C differ almost two-fold: 96.5±10.6 to 160±21.3 μM), while others (N-cadherin) are temperature independent[51]. Our ITC measurements at 10°C indicate that the pcdh-15+cdh-23 bond is entropy-driven, suggesting temperature-dependence such that its K_D could be < 1 μM at 37°C. The K_D of 2.9 μM reported here for pcdh-15+cdh-23 is in the lower range of the values measured for classical type II cadherins, although a proper comparison would require matching techniques and experimental conditions.

Predictions from simulations, tip link mechanics, and physiological time scales

Molecular dynamics simulations have usually been limited to nanoseconds, with SMD simulations using non-physiological stretching speeds to induce conformational changes within this achievable time scale[42]. However, even when using such fast pulling speeds, SMD simulations have correctly predicted the mechanical properties of multiple proteins, such as ankyrin[53] and C-cadherin[43], as determined by subsequent (independent) AFM experimental work pulling directly on them[54-56]. Transduction in the auditory system can be extremely fast[57] (< 10 μs), presenting an interesting challenge for both SMD simulations and AFM experiments. *In vivo* laser-velocimetry measurements of basilar membrane mechanics (10 to 100 dB at or near the 10 kHz characteristic frequency)[23] show motion at speeds of 10^{-5} to 10^{-2} nm/ns. In addition, experimental stimulation of hair-cell bundles is usually performed at speeds that can reach up to 0.018 nm/ns[24]. We therefore reduced the simulated stretching speed to 0.02 nm/ns, extending the time scale of our simulations to hundreds of nanoseconds (15 ns/day of computing). Thus, the SMD simulations reported here explore the response of tip-link proteins to stimuli like those of loud sound, while still providing insights into the force-bearing elements of the bond formed by pcdh-15 and cdh-23. Alternative pulling experiments can only complement our results, as the AFM cantilever can only reach pulling speeds < 10^{-5} nm/ns, covering low frequency or weak sound-like stimuli. In addition, these types of experiments only provide limited information about the structural and molecular details of forced unbinding and unfolding pathways. While our simulation results are still limited by force-field imperfections and model assumptions[58], we expect that they will guide the interpretation of the experimental exploration of the tip link's mechanical properties and the pcdh-15+cdh-23 bond.

Dynamics of pcdh-15 and cdh-23 contacts during unbinding

Trajectories of pcdh-15+cdh-23 forced unbinding were monitored to determine which molecular events were correlated with detachment and associated force peaks. In all our simulations with bound Ca^{2+}, full detachment of one protomer from the other was

preceded by rupture of contacts other than those mediated by residues near R113 in pcdh-15 (see green arrows in Fig. 3a and Supplementary Fig. 10a), by sliding of residues located near a 3_{10} helix within strand A of cadherin-23 EC1 (Y16, L18) over the RXGPP loop of pcdh-15 (Fig. 3a,b and Supplementary Fig. 10a-c), and finally by rupture of the pcdh-15_{R113} – cdh-23_{E77} salt bridge. In some cases further transient and weak interactions between the N-termini of pcdh-15 and cdh-23 ensued. We further analyzed the two slowest SMD simulations, SN6 and SNA7, which started from different initial conditions, by monitoring distances between residues at four locations: the tip of pcdh-15 and the adjacent EC2 repeat of cdh-23 (pcdh-15_{T106} – cdh-23_{L145}); the center of the interface (pcdh-15_{R113} – cdh-23_{E77} and pcdh-15_{I22} – cdh-23_{Y16}); and the tip of cdh-23 and the adjacent residues in pcdh-15 (pcdh-15_{R84} – cdh-23_{N96}). Distances plotted in Supplementary Fig. 11 confirmed the sequence of events described above. While the pcdh-15_{R113} – cdh-23_{E77} salt bridge seems to break last, it is unclear whether its head-to-head conformation facilitates sliding or actually provides resistance during unbinding. Interestingly, unbinding forces for all simulations in which the complex was equilibrated over 1 μs were slightly larger than those monitored for simulations in which the same complex was equilibrated for only 1 ns. This was correlated with an increase in interface area during equilibration (Supplementary Fig. 14).

Unbinding and unfolding of tip-link EC repeats

In simulations performed with Ca^{2+}-bound proteins, unbinding forces between pcdh-15 and cdh-23 are smaller than forces required to unfold EC1+EC2 repeats[16]. Therefore, under normal conditions, our simulations predict that the two tip-link cadherins unbind before either unfolds. However, pcdh-15+cdh-23 unbinding forces are similar to unfolding forces in the absence of Ca^{2+}. Thus unfolding may occur before unbinding when EC repeats cannot bind Ca^{2+}. Indeed, stretching simulations of the Ca^{2+}-free complex showed unfolding of EC repeats before unbinding at almost all stretching speeds (Supplementary Fig. 17). At the slowest stretching speed (0.1 nm/ns), the complex separated before EC repeats unfolded, yet linker regions in both protomers were completely extended and exposed with partial unfolding of some β-strands before complex separation. Deafness mutations impairing Ca^{2+} binding in EC repeats not directly involved in the interface between protocadherin-15 and cadherin-23 may weaken the tip-link without affecting complex formation, by promoting unfolding before unbinding upon mechanical stimulation[43,59]. The exposure of the naked linkers and unfolding of repeats might also have deleterious effects in the long term, with mis-refolding or enzyme-mediated degradation causing malfunction of tip-links with impaired Ca^{2+}-binding capabilities.

Molecular mechanisms of Ca^{2+} dependence

To reveal the molecular mechanisms underlying dissociation upon Ca^{2+} removal we performed microsecond-long molecular dynamics simulations[44] of the pcdh-15+cdh-23 structure S1b. Simulations with bound Ca^{2+}, lasting over 1 μs, showed a stable system with RMSD values < 4.4 Å for the complex, < 3 Å for cdh-23, and < 3.8 Å for pcdh-15 (Supplementary Fig. 13). In contrast, the simulated complex without bound Ca^{2+} was not stable and RMSD quickly reached values >> 5 Å. The complex did not dissociate during the simulations, but rather became deformed due to inter-repeat motion of individual

protomers (Supplementary Figs 13b,c & 14, and Movies III&IV). Individual EC repeats did retain their fold, with RMSD values not exceeding 3.6 Å (Supplementary Fig. 13d). In one of the simulations performed in the absence of Ca^{2+} we observed loss of some of the native contacts seen in the crystal structure (Supplementary Movie V). Thus, the complex may unbind in the absence of Ca^{2+} at longer time scales as a consequence of the increased dynamics of individual components (entropic stress). Unbinding may also be accelerated by other factors such as tension in the tip link. Overall, the simulations predict the existence of a transient Ca^{2+}-free complex and show how Ca^{2+} provides rigidity for each EC1-EC2 linker, which in turn maintains the binding interface of pcdh-15+cdh-23. Loss of Ca^{2+} from sites 1, 2 and 3 makes the EC-EC junction less rigid, and flexion then distorts the binding interface. This mechanism may apply to classical cadherins as well[25,60-62], where transient Ca^{2+}-free dimers have been recently reported[63,64].

Molecular mechanisms underlying inherited deafness

Four deafness mutations are located within the crystallized pcdh-15+cdh-23 complex: pcdh-15_{D157G}, cdh-23_{D101G}, pcdh-15_{R113G}, and cdh-23_{S47P}. Pcdh-15 residue D157 coordinates Ca^{2+} at site 3 and D157G may severely impair folding and/or Ca^{2+} binding, as has been shown for an equivalent D134A mutation in N-cadherin[65]. Consistently, the pcdh-15_{D157G} fragment did not co-refold with wild-type cdh-23 (Supplementary Fig. 2c). The cdh-23 D101 sidechain coordinates Ca^{2+} at site 2 and we showed experimentally[16] that D101G decreases affinity for Ca^{2+}. Although D101 is at the interface between pcdh-15 and cdh-23, the sidechain does not participate in interactions with pcdh-15. Consistently, the cdh-23_{D101G} mutant co-refolded and interacted with pcdh-15 just like wild-type cdh-23 in SEC at 1 mM $CaCl_2$ (Supplementary Fig. 2c,d). Yet ITC experiments show decreased affinity between pcdh-15 and cdh-23_{D101G} (Fig. 2c). A crystal structure of pcdh-15+cdh-23_{D101G} does not show significant changes at the interface (overall backbone RMSD 0.32 Å, Supplementary Fig. 16a). Thus, increased flexibility at the linker of cdh-23, even in the presence of bound Ca^{2+}, may explain altered binding[16]. At very low Ca^{2+} concentrations, this mutation may further impair complex formation or accelerate unfolding of a tip-link EC repeat during mechanical stimulation, as seen in our SMD simulations of the complex without bound Ca^{2+} (Supplementary Discussion above and Supplementary Fig. 17). In contrast to the previous mutations and to R113G (discussed in the main text), S47P in cdh-23 did not affect complex formation with pcdh-15 in either SEC or ITC experiments (N = 0.86; K_D = 2.4 μM, T = 10°C, ΔH = 7181 cal/mol, ΔS = 51.1 cal/mol/deg; Fig. 2c and Supplementary Figs 2c,d, 8 & 16). Moreover, this mutation is not expected to affect Ca^{2+} binding as it is not located near a Ca^{2+}-binding site nor does it modify a charged residue. A crystal structure of pcdh-15+cdh-23_{S47P} does not show significant changes at the interface (overall backbone RMSD 0.2 Å). However, a β-strand forming hydrogen bond is disrupted by this mutation, with a water molecule supplying the missing interaction and pushing the backbone of S47P away from the protomer (Supplementary Fig. 16). Thus, S47P may have a more subtle effect on the structural stability of the cdh-23 EC1 repeat, or may instead disrupt protein synthesis, processing, or localization.

Interestingly, the different biochemical effects of deafness mutations studied here correlate with the severity of the inner-ear phenotype. We were unable to co-refold the

pcdh-15$_{D157G}$ fragment, which causes both profound deafness and vestibular dysfunction. Mutations pcdh-15$_{R113G}$ and cdh-23$_{D101G}$ impaired but did not abolish complex formation and Ca^{2+} binding, respectively, and both cause severe to profound deafness but without obvious phenotype in the less mechanically-demanding vestibular system[27,28]. Lastly, the cdh-23$_{S47P}$ mutation did not produce any obvious biochemical effects, but rather a subtle structural effect that is consistent with its possible role in progressive rather than severe hearing loss[29]. Our data also suggest treatments in certain cases. Increase in Ca^{2+} concentration of the endolymph, or reduced exposure to loud noise might help subjects with mutations D101G and R113G, respectively, but may not be effective for those with the D157G mutation.

Structural determinants of heterophilic contacts

Details of the interaction between pcdh-15 and cdh-23 revealed by our structure, such as the involvement of EC2 repeats, suggest that the current EC1-based phylogenetic classification of the cadherin superfamily may need adjustments, especially if used to determine which members may interact with each other. Here we highlight structural elements and sequence motifs that may define analogous heterophilic cadherin complexes. A long and stable N-terminus, along with an exposed patch of hydrophobic and charged residues, seems to be necessary for a pcdh-15+cdh-23-like heterophilic interface. In addition, key interactions and salt-bridges (such as those between R113 in pcdh-15 and E77/Q98 in cdh-23) may provide the selectivity that prevents the same antiparallel binding for homophilic complexes or favors further overlapping with specific EC repeats (Supplementary Figs 18&19). A simple protein BLAST search for sequence motifs forming the N-termini of pcdh-15 and cdh-23, as well as their heterophilic interface, reveals some candidate heterophilic complexes. While the RXGPP loop at the N-terminus of pcdh-15 is rather unique among cadherins, the pcdh-15 EV***R***IVVR motif with R113 in the middle (Fig. 2h) is also found in *Mus musculus* fat4 at the same location in EC1 (EV***R***VLVR). Similarly, a search for the cdh-23 KV***N***I***Q***V motif with interfacial residues N96 and Q98 (Fig. 2h) reveals an *identical* motif in EC1 of *Mus musculus* fat3. Interestingly, the cdh-23 KS***E***FT motif with the interfacial residue E77 is also similar to the Q***DN***YL at the same location in EC1 of fat3. These facts, and sequence alignments (data not shown), suggest that fat4 and fat3 share several features important for heterophilic interactions. Analysis of pcdh-21 and pcdh-24 sequences reveals similarities with cdh-23, suggesting that these proteins may form heterophilic complexes with other cadherins. Evidently, a more thorough analysis with homology models is required to determine if pcdh-15+cdh-23-like complexes can be formed by fat3 and fat4, and whether pcdh-21 and pcdh-24 can form heterophilic complexes with other cadherins. However, the sequence motifs and structural elements discussed here provide a first step to search for novel heterophilic cadherin complexes and establish their biological relevance. It would be important to determine if pcdh-15 and cdh-23 can interact with other cadherin molecules as well. Protocadherin-15 is widely expressed in the brain and several tissues including kidney, lung, and pancreas[66]; it may feature polymorphisms positively selected in humans[67], and has been associated with retinal disorders, lipid abnormalities[66], and cancer[15]. The present study opens the door to exploring its function in different tissues from a structural point of view.

Supplementary Movie Legends

Movie I (A&B)

Forced unbinding of pcdh-15+cdh-23 (simulation SNA7; trajectory shown from t = 270 ns up to t = 336 ns). Protein is depicted in cartoon representation, with pcdh-15 in purple, cdh-23 in blue, and Ca^{2+} in green. C-terminal C_α atoms are red. Molecular surfaces for pcdh-15 and cdh-23 are shown in transparent purple and blue. Version B shows the same trajectory with opaque molecular surfaces.

Movie II (A&B)

Details of pcdh-15+cdh-23 forced unbinding (simulation SNA7; trajectory shown from t = 270 ns up to t = 336 ns). Protein is depicted as in Movie I, with residues at the interface shown in stick representation. Molecular surfaces are not shown in movie version A. Version B shows opaque and transparent surfaces for pcdh-15 and cdh-23, respectively.

Movie III

Equilibration of pcdh-15+cdh-23 in the presence of Ca^{2+} (simulation SA1, lasting 1 μs). Protein is depicted in cartoon representation. Pcdh-15 is in purple, cdh-23 in blue, and Ca^{2+} in green.

Movie IV

Equilibration of pcdh-15+cdh-23 in the absence of Ca^{2+} (simulation SA3, lasting 1 μs). Protein is depicted in cartoon representation and colored as in movie III.

Movie V

Dynamics of contacts between pcdh-15 and cdh-23 during equilibrium MD simulations. Contact maps between residue pairs involved in the pcdh-15+cdh-23 interface are shown throughout microsecond-long MD simulations performed in the NpT ensemble with and without Ca^{2+} (SA1 left; SA3 right). The distance between pairs of C_α atoms is displayed using a linear gray scale (0 Å: black; >10 Å: white). A red box highlights location of native contacts lost at the end of simulation SA3 without Ca^{2+}.

Supplementary Tables

Supplementary Table 1. Statistics for pcdh-15+cdh-23 structures

Data Collection and Refinement	Structure S1a	Structure S1b	Structure S2
Space group	C2	C2	C2
Unit cell parameters:			
a, b, c (Å)	173.61, 40.47, 84.62	173.65, 40.47, 85.19	158.75, 57.03, 156.16
α, β, γ (°)	90, 103, 90	90, 103, 90	90, 99, 90
Molecules per asymmetric unit	1	1	2
Beam source	APS 24-ID-E	ALS 4.2.2	APS 24-ID-E
Wavelength (Å)	0.97949	1.13841	0.97949
Resolution limit (Å)	1.65	2.23	2.63
Unique reflections	66,852 (3,184)	27,442 (1,236)	41,589 (2,017)
Redundancy	3.7 (3.6)	3.4 (2.9)	3.7 (3.6)
Completeness (%)	96.9 (92.8)	96.2 (87.5)	100 (99.8)
Average I/σ(I)	25.6 (2.8)	10.7 (2.7)	16.9 (2.6)
R_{merge}	0.05 (0.48)	0.10 (0.39)	0.08 (0.51)
Refinement			
Resolution range (Å)	32.03 - 1.65 (1.70 - 1.65)	41.08 - 2.23 (2.29 - 2.23)	38.57 - 2.63 (2.69-2.62)
Residues (atoms)	446 (4,550)	444 (3,924)	889 (7,517)
Water molecules	823	348	480
R_{work} (%)	16.1 (28.7)	17.5 (25.0)	18.9 (34.6)
R_{free} (%)	19.3 (31.7)	23.6 (31.6)	24.3 (38.8)
RMS deviations			
Bond lengths (Å)	0.010	0.017	0.010
Bond angles (°)	1.415	1.543	1.201
B-factor average			
Protein	22.49	29.53	43.18
Ligand/ion	24.52	42.16	31.07
Water	38.41	35.99	41.11
Ramachandran Plot Regions[a]			
Most favored (%)	90.7	90.7	88.5
Additionally allowed (%)	8.8	9.1	10.9
Generously allowed (%)	0.5	0.3	0.6
Disallowed (%)	0.0	0.0	0.0
Interface Area (Å^2)	907	898	1160 1069
PDB ID code	4apx	4axw	4aq8

[a]Computed with PROCHECK

Supplementary Table 2. Statistics for mutant pcdh-15+cdh-23 structures

Data Collection and Refinement	Structure S3 pcdh-15+cdh-23$_{D101G}$	Structure S4 pcdh-15+cdh-23$_{S47P}$
Space group	C2	C2
Unit cell parameters:		
a, b, c (Å)	173.29, 40.51, 84.63	174.02, 40.87, 84.78
α, β, γ (°)	90, 103, 90	90, 103, 90
Molecules per asymmetric unit	1	1
Beam source	APS 24-ID-E	APS 24-ID-E
Wavelength (Å)	0.97919	0.97919
Resolution limit (Å)	1.96	2.26
Unique reflections	41,729 (1,981)	27,207 (1,318)
Redundancy	3.4 (2.9)	3.5 (3.1)
Completeness (%)	99.4 (95.5)	99.2 (96.8)
Average I/σ(I)	8.5 (2.4)	9.6 (2.3)
R_{merge}	0.11 (0.40)	0.13 (0.44)
Refinement		
Resolution range (Å)	34.19 – 1.96 (2.00 – 1.96)	22.69 – 2.27 (2.33 – 2.27)
Residues (atoms)	443 (4,155)	444 (3,945)
Water molecules	606	403
R_{work} (%)	17.8 (22.1)	17.3 (20.2)
R_{free} (%)	22.8 (29.9)	23.9 (29.0)
RMS deviations		
Bond lengths (Å)	0.009	0.011
Bond angles (°)	1.327	1.404
B-factor average		
Protein	23.64	24.35
Ligand/ion	20.31	23.29
Water	31.97	28.24
Ramachandran Plot Regions[a]		
Most favored (%)	91.1	90.4
Additionally allowed (%)	8.3	9.4
Generously allowed (%)	0.5	0.3
Disallowed (%)	0.0	0.0
Interface Area (Å^2)	958	895
PDB ID code	4aqa	4aqe

[a]Computed with PROCHECK

Supplementary Table 3. Summary of simulations

Label	Ensemble	Ion	tsim (ns)	SMD Speed (nm/ns)	Start	Size (# atoms)	Size (nm^3)
SN1	NpT	Ca^{2+}	1.1[a]	-	-	195,123	26.6 x 9.6 x 8.1
SN2	NVE	Ca^{2+}	1.5	10	SN1		
SN3	NpT	Ca^{2+}	1.4	10	SN1		
SN4	NVE	Ca^{2+}	7.1	1	SN1		
SN5	NpT	Ca^{2+}	6.6	1	SN1		
SN6	NpT	Ca^{2+}	53.4	0.1	SN1		
SN7	NpT	Ca^{2+}	1.1[a]	-	-	108,720	15.0 x 9.6 x 8.1
SN8	NpT	K^+	1.1[a]	-	-	108,722	
SN9	NpT	Ca^{2+}	1.1[a]	-	-	221,389	27.0 x 9.8 x 8.8
SN10	NVE	Ca^{2+}	1.5	10	SN9		
SN11	NpT	Ca^{2+}	1.5	10	SN9		
SN12	NVE	Ca^{2+}	9.5	1	SN9		
SN13	NpT	Ca^{2+}	6.3	1	SN9		
SA1	NpT	Ca^{2+}	1000.0	-	SN7	108,720	15.0 x 9.6 x 8.1
SA2	NVT	Ca^{2+}	2000.0	-	SN7		
SA3	NpT	K^+	1000.0	-	SN8	108,722	
SA4	NVT	K^+	2000.0	-	SN8		
SNA1	NpT	Ca^{2+}	5.1[a]	-	SA1[b]	193,446	26.6 x 9.6 x 8.1
SNA2	NVE	Ca^{2+}	1.5	10	SNA1		
SNA3	NpT	Ca^{2+}	1.5	10	SNA1		
SNA4	NVE	Ca^{2+}	10.6	1	SNA1		
SNA5	NpT	Ca^{2+}	9.8	1	SNA1		
SNA6	NpT	Ca^{2+}	78.6	0.1	SNA1		
SNA7	NpT	Ca^{2+}	336.1	0.02	SNA1		
SNA8	NpT	K^+	5.1[a]	-	SA3[b]	190,180	26.6 x 9.6 x 8.1
SNA9	NVE	K^+	1.5	10	SNA7		
SNA10	NpT	K^+	1.5	10	SNA7		
SNA11	NVE	K^+	13.0	1	SNA7		
SNA12	NpT	K^+	10.4	1	SNA7		
SNA13	NpT	K^+	74.6	0.1	SNA7		
SNA14	NpT	Ca^{2+}	1.1[a]	-	SA1[b]	377,668	26.0 x 9.5 x 16.1
SNA15	NVE	Ca^{2+}	2.0	10	SNA14		
SNA16	NpT	Ca^{2+}	1.6	10	SNA14		
SNA17	NVE	Ca^{2+}	10.3	1	SNA14		
SNA18	NpT	Ca^{2+}	9.3	1	SNA14		
SNA19	NpT	Ca^{2+}	74.3	0.1	SNA14		
SNC1	NpT	Ca^{2+}	1.1[a]	-	-	203,769	27.8 x 9.4 x 8.2
SNC2	NVE	Ca^{2+}	1.9	10	SNC1		
SNC3	NpT	Ca^{2+}	1.8	10	SNC1		
SNC4	NVE	Ca^{2+}	8.0	1	SNC1		
SNC5	NpT	Ca^{2+}	7.4	1	SNC1		
SNC6	NpT	Ca^{2+}	69.0	0.1	SNC1		
SNC7	NpT	Ca^{2+}	257.6	0.02	SNC1		

[a]These simulations consisted of 1,000 steps of minimization, 100 ps of dynamics with the backbone of the protein restrained (k = 1 Kcal/mol/$Å^2$), and the remaining time as free dynamics in the NpT ensemble (γ=0.1 ps^{-1}).
[b]Coordinates of the final snapshot of SA1 or SA3 were used to build a system with a larger water box for SMD.

Summary of pcdh-15+cdh-23 and C-cadherin simulations. Labels indicate simulation platform (SN: NAMD; SA: Anton; SNA: NAMD after Anton). C-cadherin simulations are labeled SNC. Ensembles are denoted according to the thermodynamic quantities held constant (N: # atoms; p: pressure; T: temperature; V: volume; E: Energy). Occupancy of binding sites at the beginning of the simulations is indicated in Ion column. Initial coordinates and velocities (when applicable) were obtained from the last frame of the simulations indicated in the Start column. Initial size of the system (in nm^3) is indicated in the last column. All pcdh-15+cdh-23 simulations used structure S1b, except for simulations SN9 to SN13, which used structure S1a.

Supplementary Figures and Legends

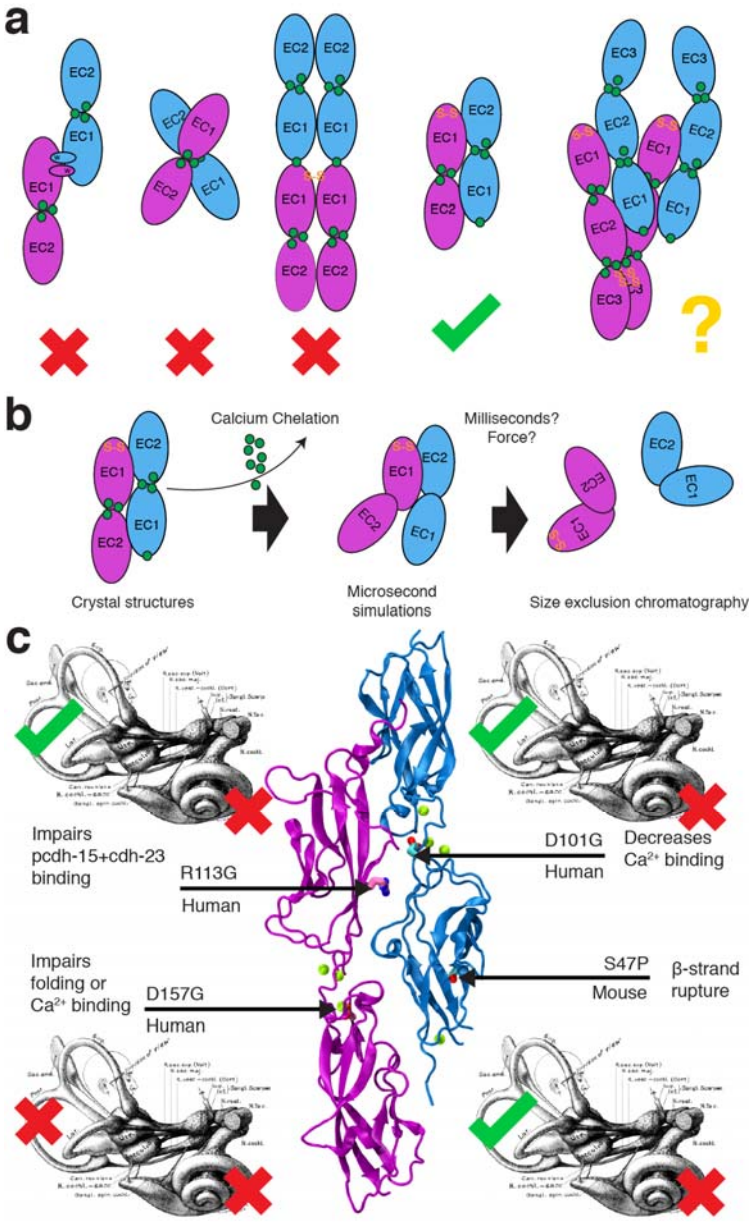

Supplementary Figure 1. Structural determinants of tip-link function in hearing and deafness. **a**, The bond formed by protocadherin-15 and cadherin-23 does not involve β-strand exchange or formation of an X-dimer as in classical cadherins[50,68-70], and is not directly mediated by Ca^{2+} as previously suggested[16,17]. An overlapped antiparallel dimer involving the N-terminal EC1+2 repeats of each protein forms the protocadherin-15 and cadherin-23 bond. Parallel homodimerization is likely mediated by other repeats beyond EC2 in each protein. **b**, Ca^{2+} chelation promotes disassembly of the pcdh-15+cdh-23 bond, as determined by SEC experiments. Microsecond-long molecular dynamics simulations suggest that removal of Ca^{2+} results in entropic stress, which may lead to complex separation over a longer time scale or may facilitate disassembly by mechanical force. A transient, Ca^{2+}-free complex is predicted to exist. **c**, Deafness-related mutations are located in the pcdh-15+cdh-23 structure. Known phenotype (auditory and/or vestibular) is indicated along with structural defects suggested by our biochemical experiments, presented here and in ref 16.

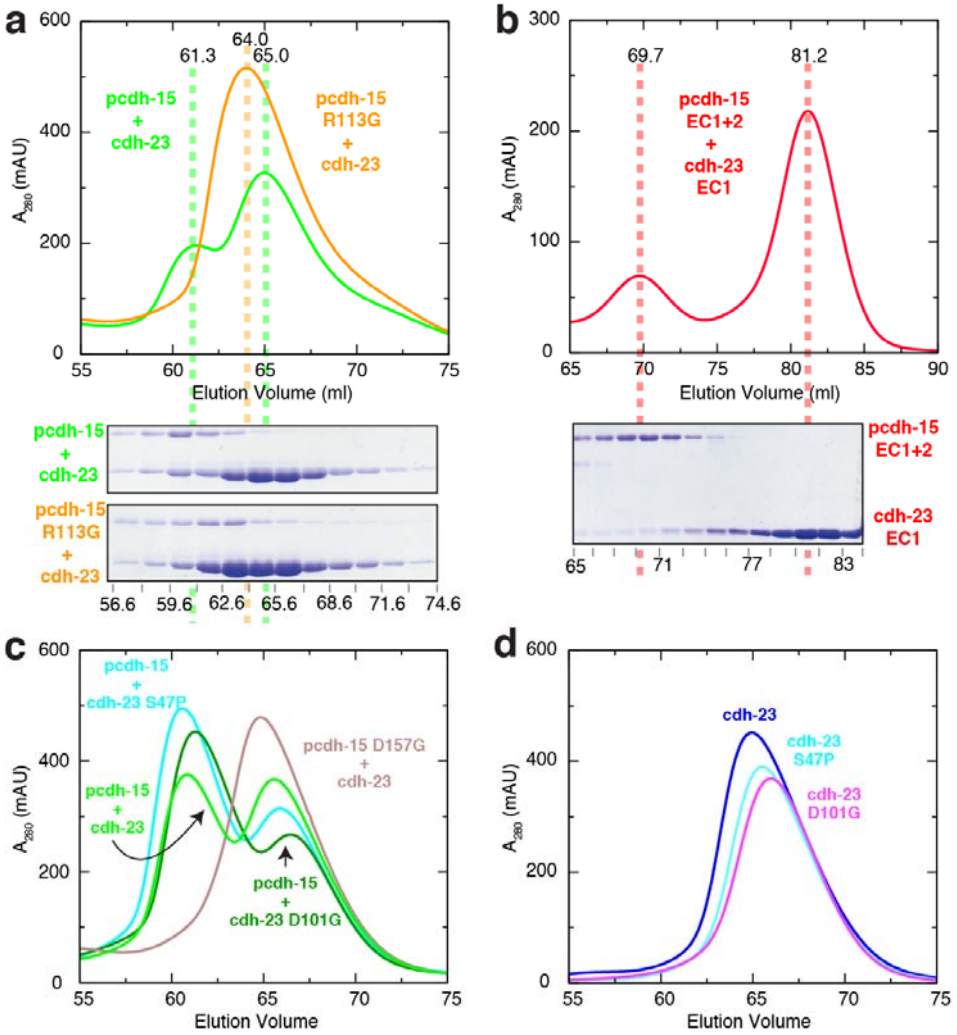

Supplementary Figure 2. SEC of co-refolded protocadherin-15 and cadherin-23 fragments. **a**, Representative traces for wild-type protocadherin-15 EC1+2 co-refolded with cadherin-23 EC1+2 (pcdh-15+cdh-23, green), and mutant pcdh-15_{R113G} co-refolded with cdh-23 (pcdh-15_{R113G}+cdh-23, orange). Experiments were performed using a Superdex S75 16/60 column. Coomassie-stained SDS-PAGE analysis of eluted fractions is shown below the chromatogram. Trace for co-refolded pcdh-15+cdh-23 (green) shows two peaks; the first one, at 61.3 ml, contained both proteins (complex) and was used for crystallization. The second peak (65 ml) contained cdh-23 alone. Trace for co-refolded pcdh-15_{R113G}+cdh-23 shows a single peak with no obvious shift in elution volume for protein fragments. **b**, Representative trace for wild-type pcdh-15 co-refolded with cadherin-23 EC1 (red). The two protein fragments eluted independently from each other in two peaks (69.7 ml and 81.2 ml) as indicated by Coomassie-stained SDS-PAGE of the eluted fractions shown beneath the chromatogram. Similar results were obtained for pcdh-15_{R113G} and pcdh-15_{I22A}. Fractions from the first peak were used for further SEC or ITC (Figs 2 & 4). **c**, SEC of co-refolded wild-type pcdh-15+cdh-23 and mutants involved in inherited deafness. Traces indicate that mutations D101G and S47P in cdh-23 did not prevent complex formation. SEC of co-refolded pcdh-15_{D157G} + cdh-23 shows a single peak with negligible amounts of pcdh-15_{D157G}. **d**, SEC traces of refolded wild-type cdh-23 and mutants show single monodisperse peaks for all samples. All SEC experiments in this figure were performed in the presence of 1 mM $CaCl_2$.

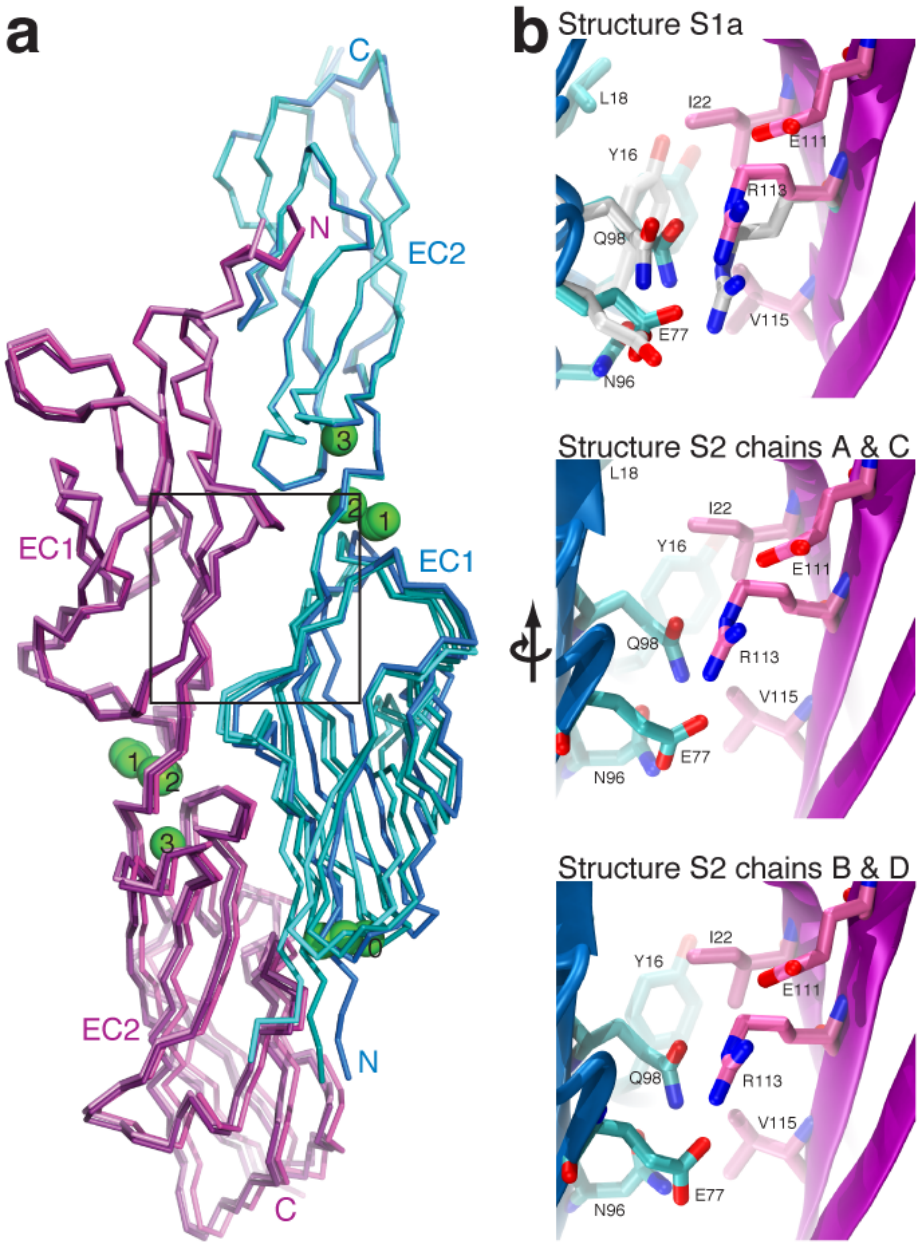

Supplementary Figure 3. Pcdh-15+cdh-23 structures showed nearly identical conformations for individual pcdh-15 and cdh-23 fragments with flexing at the linker regions (up to ~10°). **a**, Superposition of the S1a structure (darker colors) and the two complexes in the asymmetric unit of the S2 structure. The three structures were superimposed on the cdh-23 EC2 repeat to highlight the slight linker flexibility that results in mostly coordinated displacement of the EC1 repeat of cdh-23 and the EC2 repeat of pcdh-15. The buried surface area of the three complexes is 907 Å^2 for S1a, 1069 Å^2 for S2 chains A and C, and 1160 Å^2 for S2 chains B and D. The three structures are shown as C_α traces, with pcdh-15 in purple, cdh-23 in blue and Ca^{2+} ions as green spheres. Box indicates the approximate position of the detail shown in (b). **b**, Detail of interface between pcdh-15 and cdh-23 for the three structures superimposed in (a). This region of the interface is centered on residue R113, which when mutated causes deafness. Protein backbone and surrounding residues are shown in cartoon (pcdh-15, purple; cdh-23, blue) and sticks (pcdh-15, pink; cdh-23, cyan). In the top panel, the high-resolution structure showed alternative conformations for a few sidechains, shown in gray.

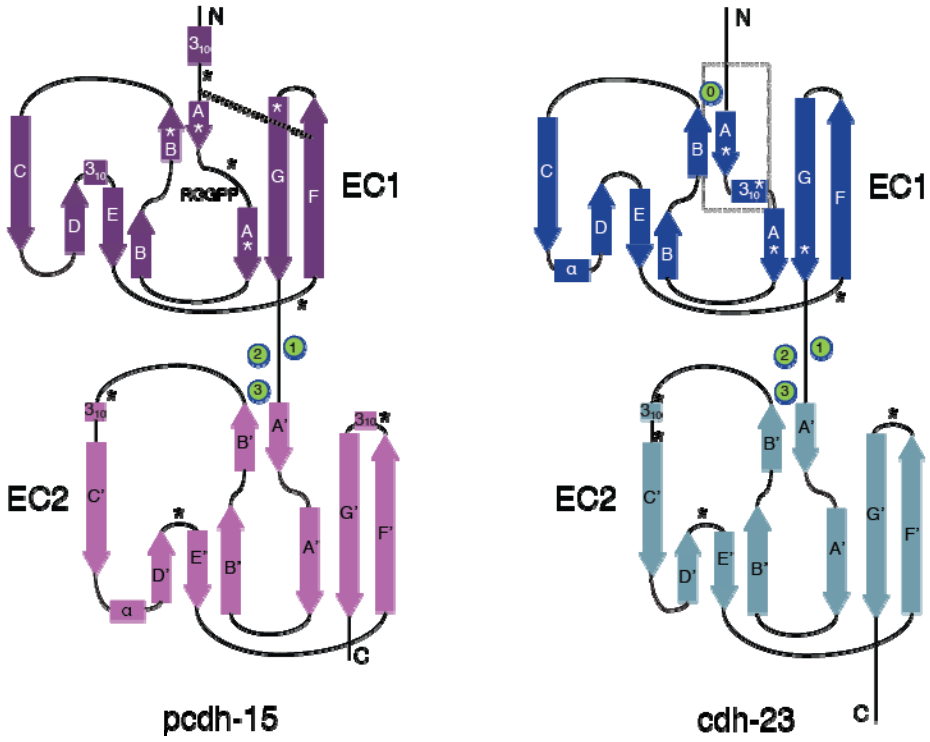

Supplementary Figure 4. Topology diagrams for pcdh-15 and cdh-23. Protocadherin-15 repeats EC1 and EC2 feature typical cadherin folds with seven β-strands labeled A to G. Pcdh-15 EC1 features a 3_{10} helix and the C11-C99 disulfide bond (dashed line) linking β-strands F and A at the N-terminus. Regions involved in heterophilic interactions are indicated with an asterisk (*).

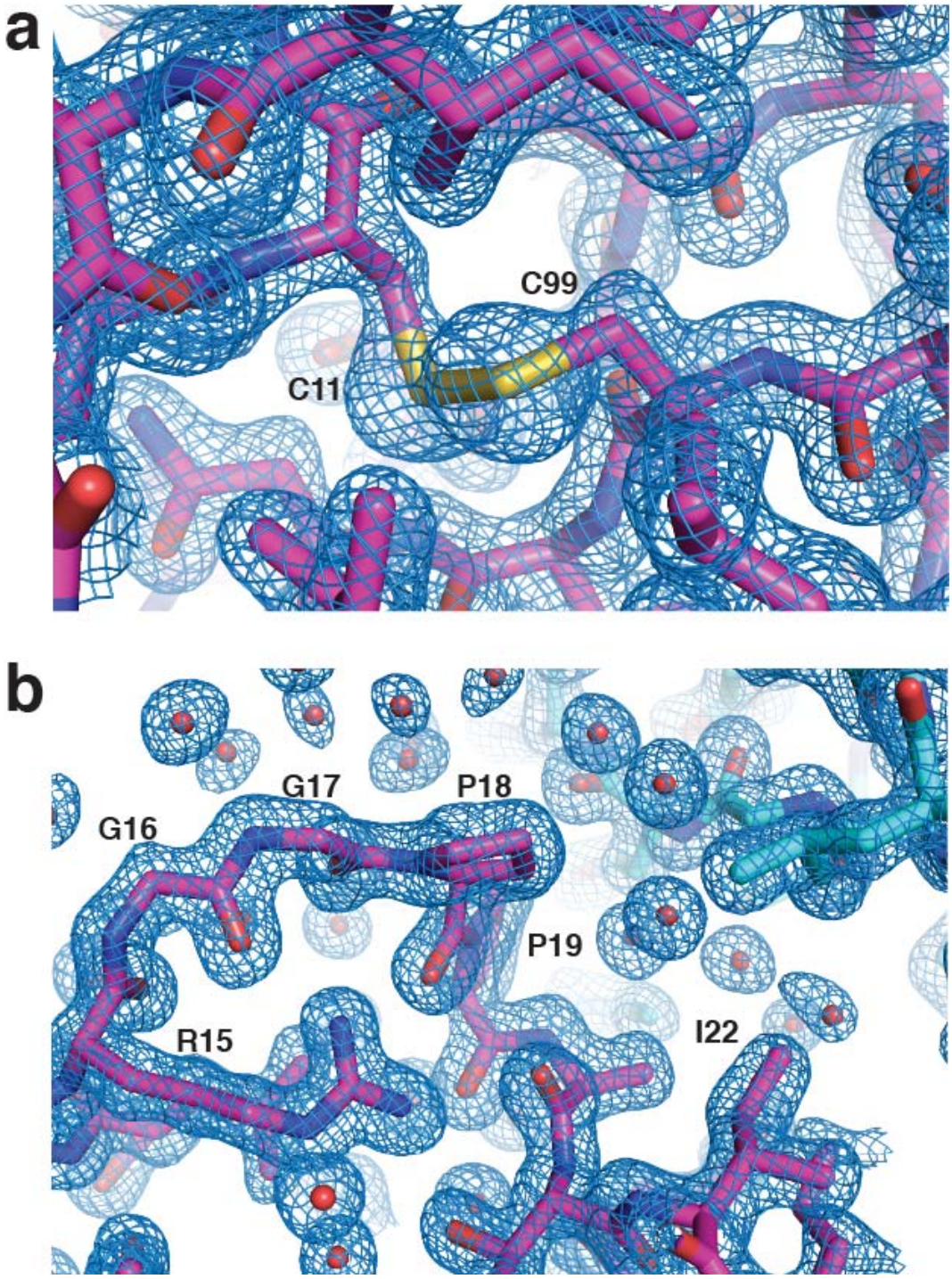

Supplementary Figure 5. Unique structural features of pcdh-15. Weighted $2F_o$-F_c electron density map from the S1a structure contoured at 1.5σ. **a**, The disulfide bond linking C11 and C99 clamps the N-terminal end of the EC1 β-sandwich. **b**, The RXGPP loop is buttressed by interactions of the arginine sidechain with the carbonyl groups of both prolines. Pcdh-15 is shown in magenta and cdh-23 in cyan.

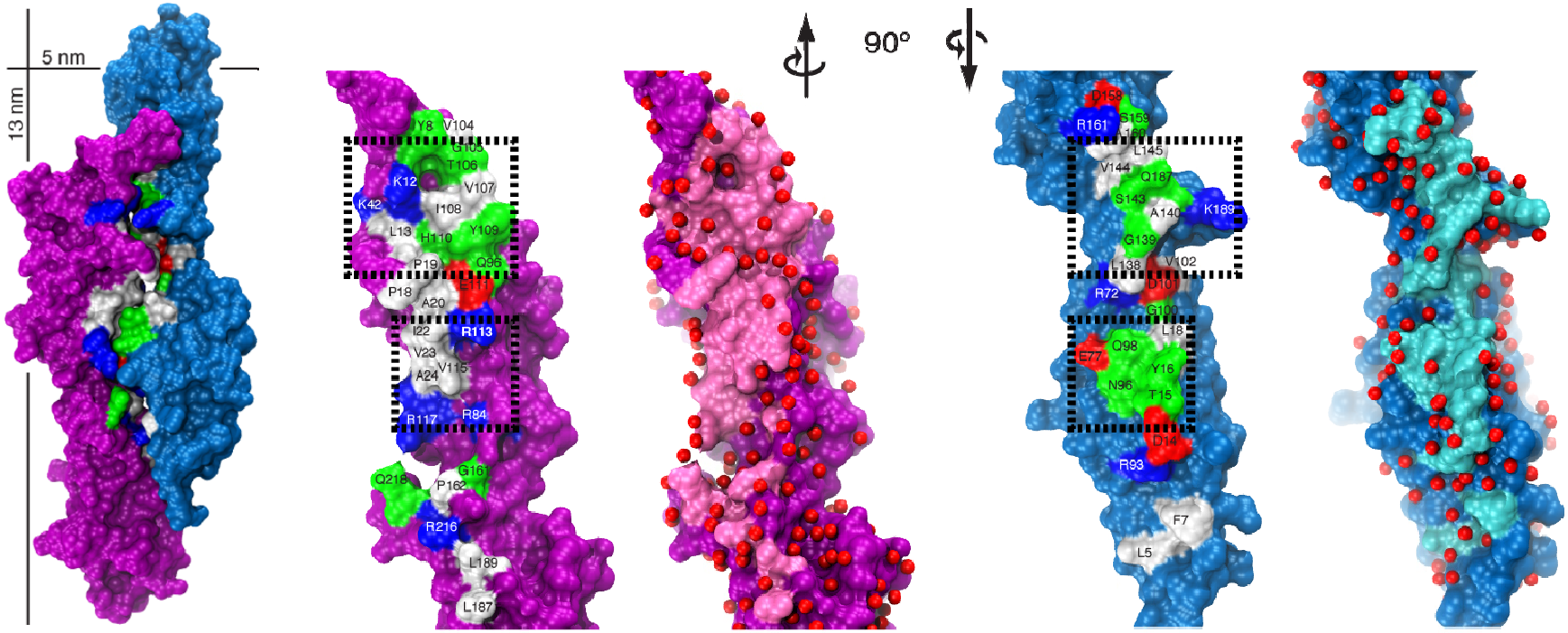

Supplementary Figure 6. Features of the pcdh-15+cdh-23 interface. Molecular surface representation of pcdh-15 (purple) and cdh-23 (blue). The interaction surfaces are also exposed with interfacing residues labeled and colored according to residue type (white: apolar; green: polar; red: negatively charged; blue: positively charged). Water molecules (red spheres) within 3 Å of each protomer are shown with interfacing residues colored in pink (pcdh-15) and cyan (cdh-23). Dashed boxes indicate the two main areas of interaction.

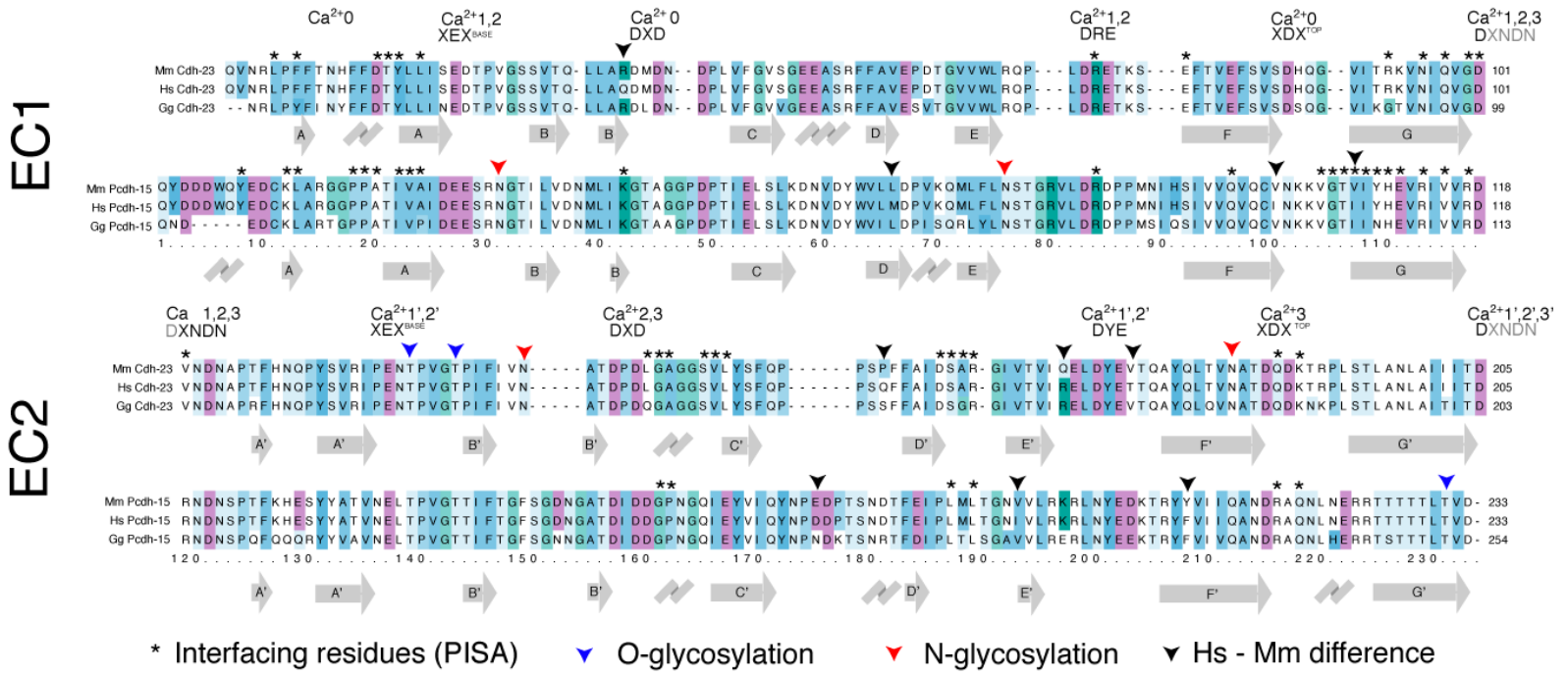

Supplementary Figure 7. Alignment of cadherin-23 and protocadherin-15 sequences for repeats EC1 (top) and EC2 (bottom) corresponding to *Mus musculus* (Mm), *Homo sapiens* (Hs), and *Gallus gallus* (Gg). NCBI reference sequences: NP_075859.2, NP_071407.4, XP_421595.2; NP_001136218.1, NP_001136235.1, NP_001038119.1. Conserved Ca^{2+}-binding motifs are labeled XEX^{BASE}, DXD, DRE, XDX^{TOP}, and DXNDN. Black arrowheads indicate differences between *Mus musculus* and *Homo sapiens* sequences. Interfacing residues are indicated with an asterisk (*). Blue and red arrowheads indicate predicted O- and N-glycosylation sites. Secondary structure is indicated below the alignment for each protein.

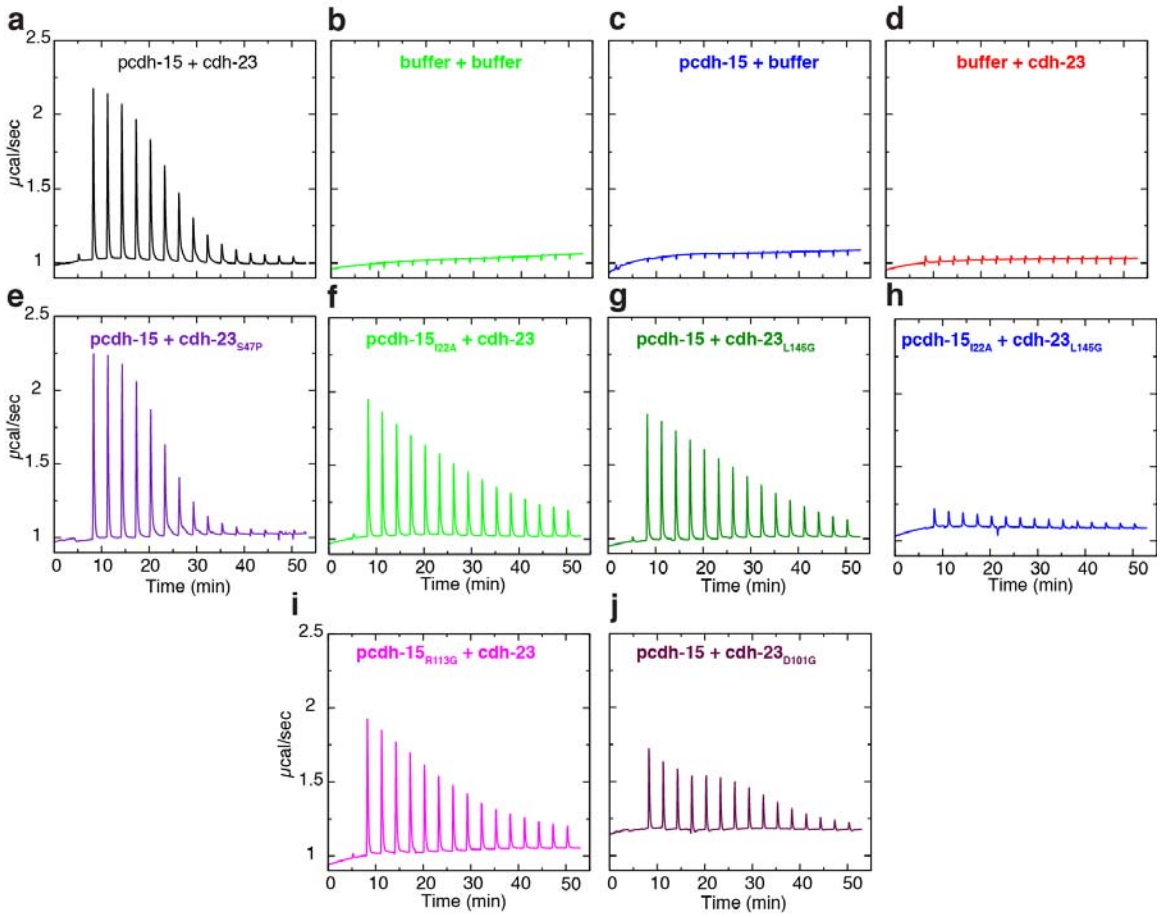

Supplementary Figure 8. Pcdh-15+cdh-23 complex formation probed using isothermal titration calorimetry (ITC) and site-directed mutagenesis. Raw power vs time data are shown for: **a,** pcdh-15 (111 μM) titrated with cdh-23 (1.1 mM, same as in Fig. 2a); **b**, buffer titrated with buffer (control); **c**, pcdh-15 (111 μM) titrated with buffer (control); **d**, buffer titrated with cdh-23 (1.1 mM, blank); **e**, pcdh-15 (120 μM) titrated with cdh-23_{S47P} (1.2 mM); **f**, pcdh-15_{I22A} (110 μM) titrated with cdh-23 (1.1 mM); **g**, pcdh-15 (130 μM) titrated with cdh-23_{L145G} (1.2 mM); **h**, pcdh-15_{I22A} (114 μM) titrated with cdh-23_{L145G} (1.2 mM, same as in Fig. 2a); **i**, pcdh-15_{R113G} (110 μM) titrated with cdh-23 (1.1 mM); **j**, pcdh-15 (156 μM) titrated with cdh-23_{D101G} (1.2 mM). All experiments were performed at 10°C with matched buffers.

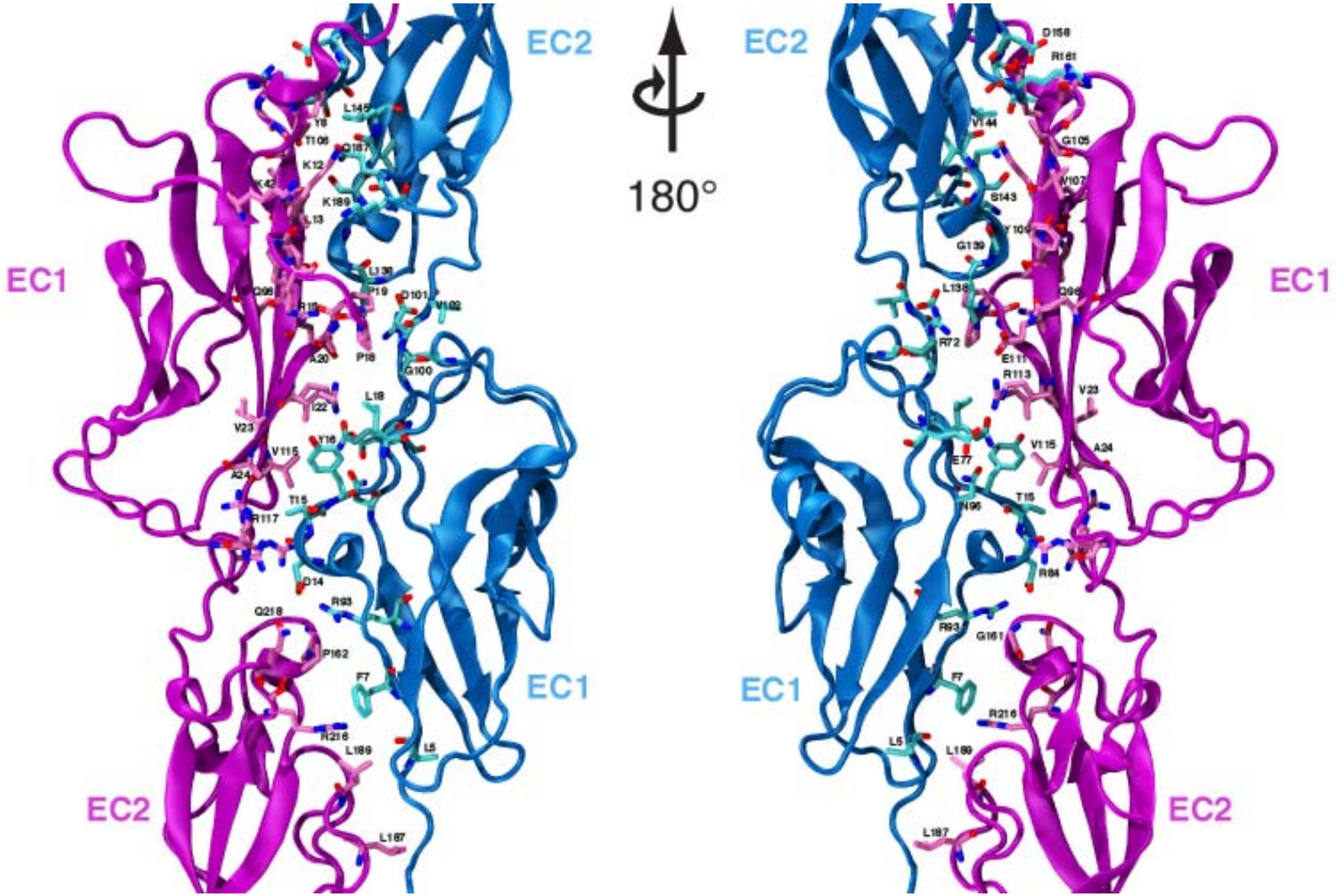

Supplementary Figure 9. Details of the pcdh-15+cdh-23 interface. Two views of a ribbon diagram of pcdh-15 (purple) and cdh-23 (blue) with interfacing residues labeled and shown in stick representation.

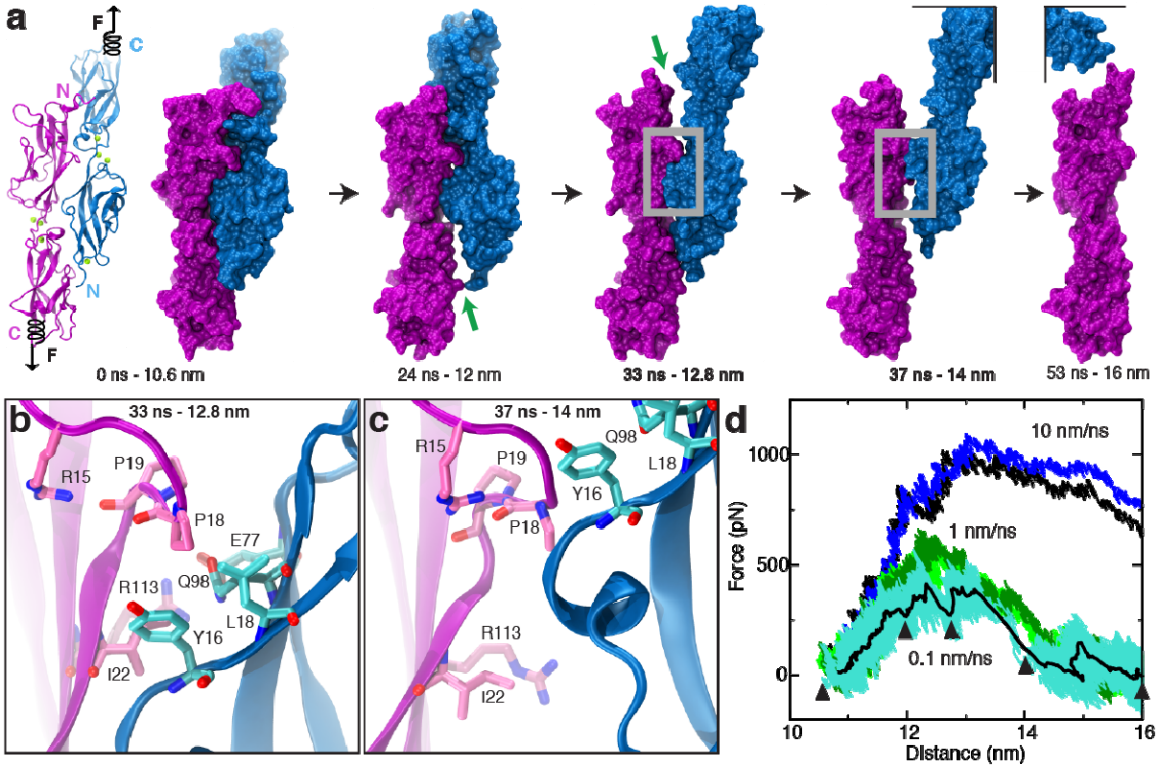

Supplementary Figure 10. Mechanical strength of the pcdh-15+cdh-23 complex probed by SMD simulations. **a**, Snapshots of pcdh-15 (purple) and cdh-23 (blue) unbinding during simulation SN6 (Supplementary Table 3). The protein complex is shown in both cartoon and surface representations at the beginning of the simulation, and then in surface representation at indicated time points. Ca^{2+} ions are shown as green spheres. Force was applied to the C-termini of both protomers. Complete complex separation was achieved after 50 ns. Green arrows point to broken interfaces; gray boxes are detailed in **b-c**, showing interacting residues before and after sliding during unbinding. **d**, Force applied to one C-terminus versus distance between C-termini ends of pcdh-15 and cdh-23. Different traces correspond to independent simulations performed at stretching speeds of 10 (blue and black), 1 (light and dark green), and 0.1 nm/ns (cyan). Snapshots in (a) are indicated by arrowheads. A 1-ns running average of the cyan curve is shown in black. At least one clear unbinding force peak was discernable in each simulation.

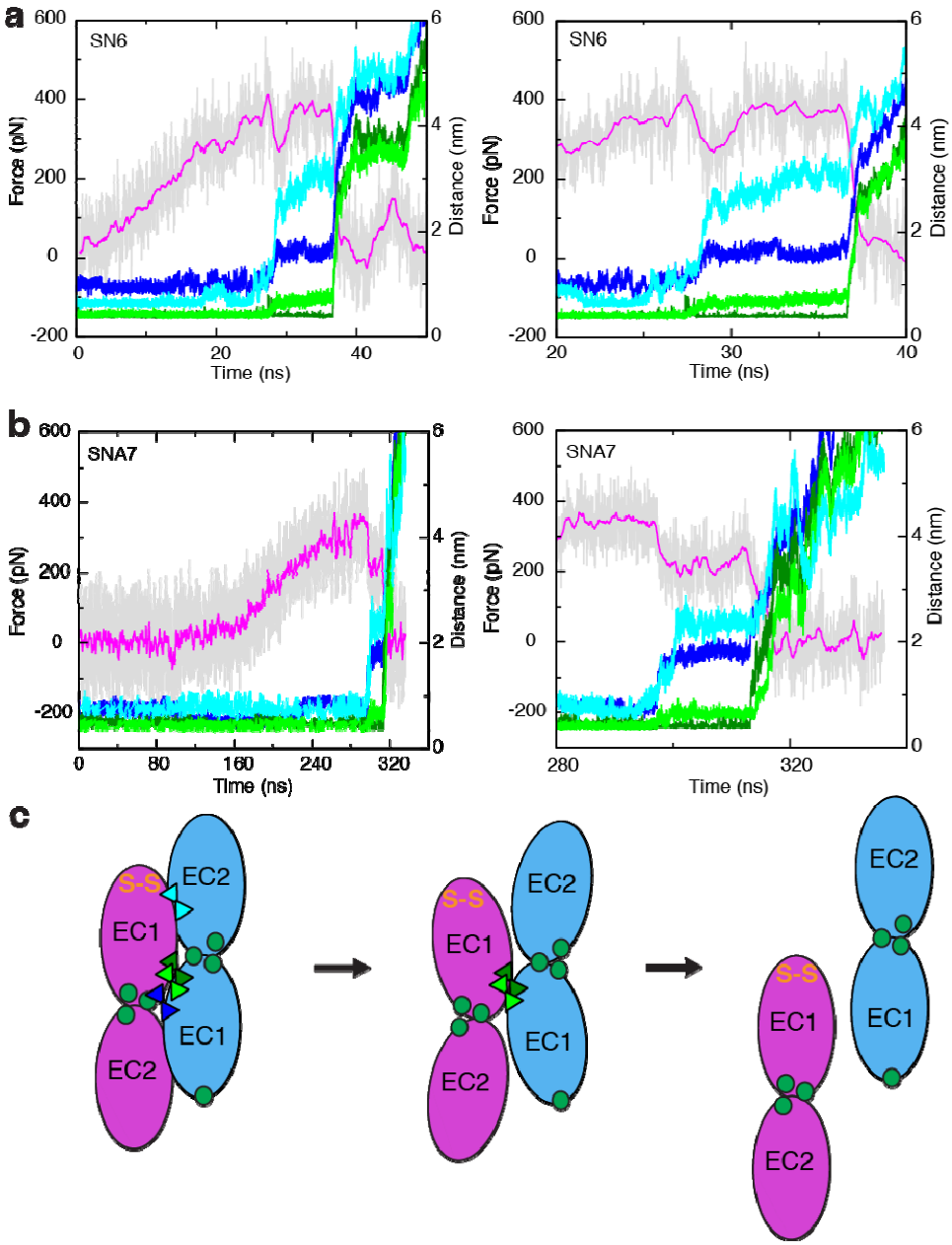

Supplementary Figure 11. Molecular correlates of pcdh-15+cdh-23 forced unbinding. **a-b**, Force (left scale) applied to one of the protein complex C-termini along with distances between residues versus time for simulations SN6 and SNA7, respectively. Force is shown in gray, with 1-ns running average in magenta. Distances (right scale) were monitored throughout SMD simulations at four locations: the tip of pcdh-15 and the adjacent EC2 repeat of cdh-23 (pcdh-$15_{T106}C_{\beta}$ – cdh-$23_{L145}C_{\gamma}$ in cyan); the center of the interface (pcdh-$15_{R113}C_{\zeta}$ – cdh-$23_{E77}C_{\delta}$ in dark green and pcdh-$15_{I22}C_{\beta}$ – cdh-$23_{Y16}C_{\zeta}$ in light green); and the EC1 repeat of cdh-23 and the adjacent residues in pcdh-15 (pcdh-$15_{R84}C_{\zeta}$ – cdh-$23_{N96}C_{\gamma}$ in blue). Right panels show detail during unbinding, highlighting a sequential separation with detachment of bonds in green occurring last. **c**, Schematic location of bonds described in (a) and (b) throughout forced unbinding.

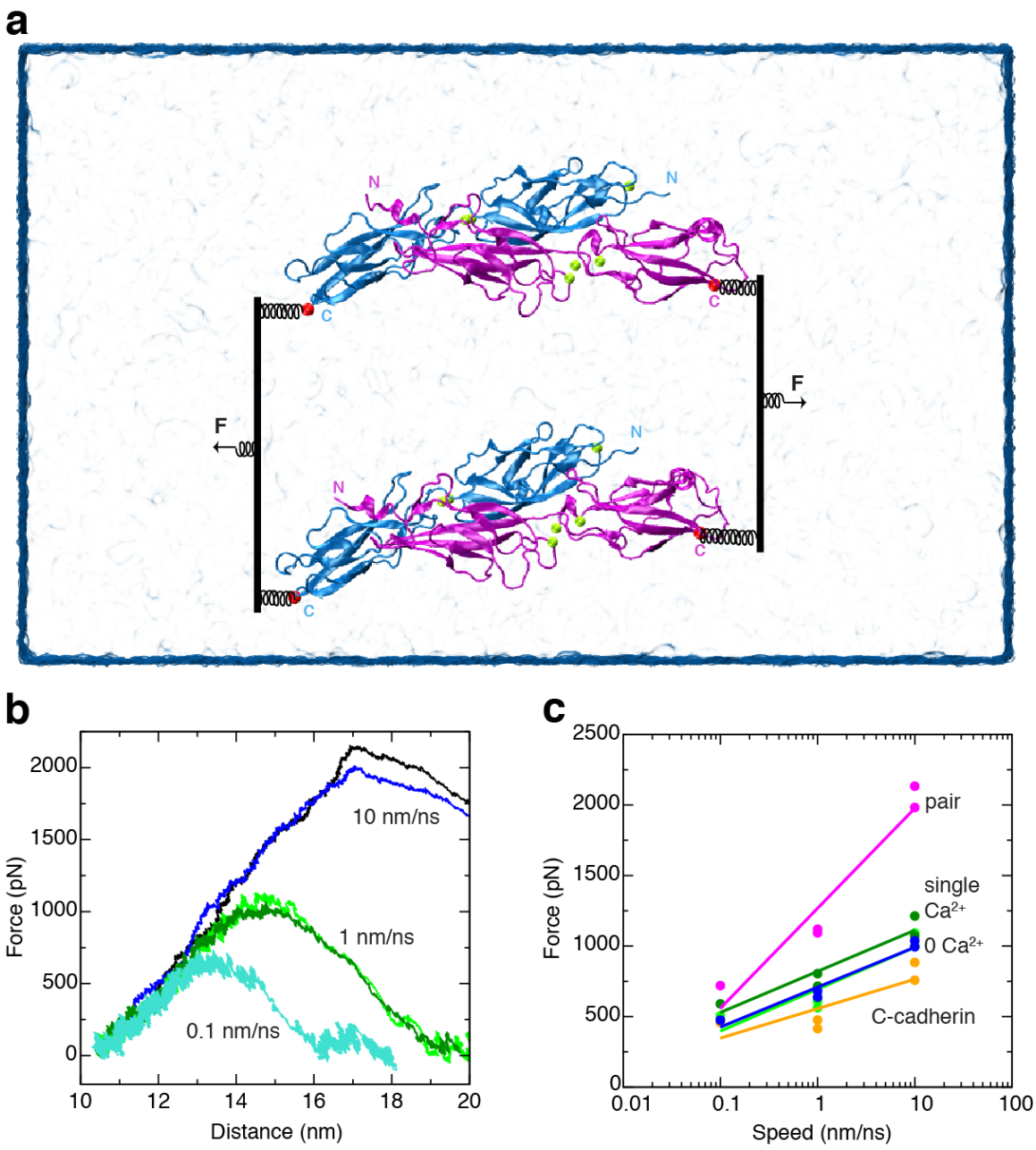

Supplementary Figure 12. Mechanical strength of two pcdh-15+cdh-23 complexes in parallel. **a**, System setup. Two pcdh-15+cdh-23 complexes were placed in parallel but far from each other in a large water box. The C-termini of the two pcdh-15 protomers were connected to a virtual slab through independent springs with spring constants equivalent to two EC repeats each. The slab was in turn connected to an SMD atom moving at constant velocity (all forces were applied in the stretching direction only). A similar arrangement was set for the C-termini of cdh-23. **b**, Force applied to one of the slabs versus distance between slabs. Different traces correspond to independent simulations performed at stretching speeds of 10 (blue and black), 1 (light and dark green), and 0.1 nm/ns (cyan). **c**, Maximum force-peak values vs. stretching speed for unbinding simulations of the pair of complexes shown in magenta (simulations SNA15 to SNA19). Unbinding force-peak values for simulations of single complexes with (green) and without Ca^{2+} (blue), as well as for C-cadherin (SNC2 to SNC6, orange) are shown for reference.

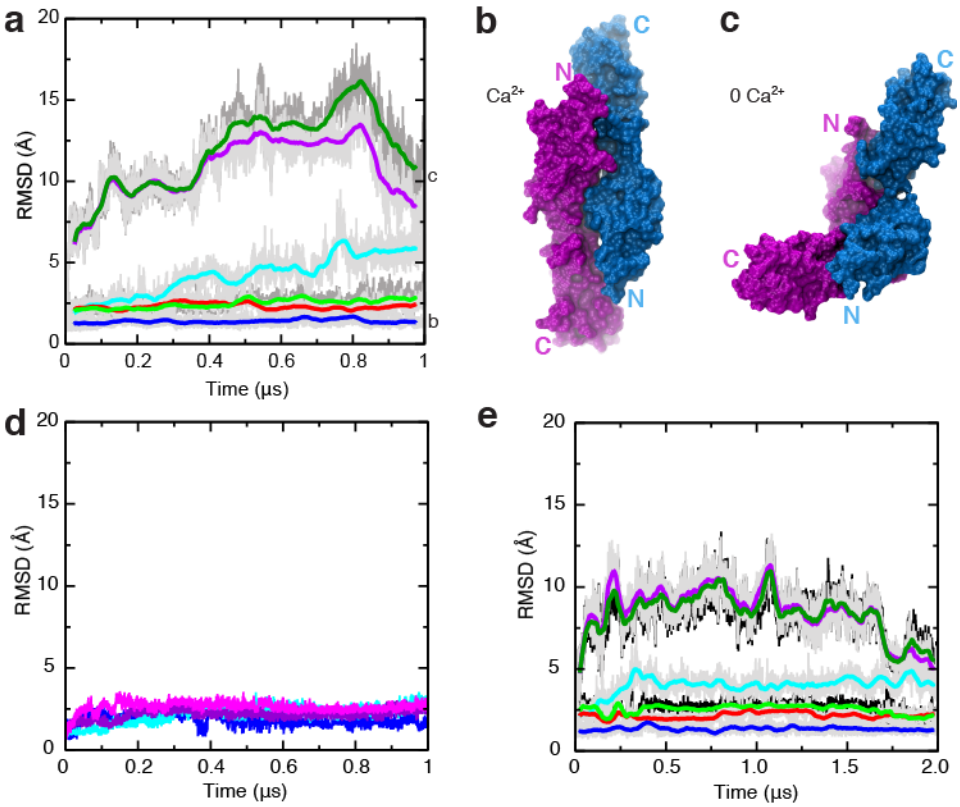

Supplementary Figure 13. Removal of bound Ca^{2+} causes complex instability in simulations. **a**, RMSD versus time for simulations SA1 and SA3 in the NpT ensemble (Supplementary Table 3) of the cdh-23+pcdh-15 complex in the presence (light green, whole complex; red, pcdh-15; blue, cdh-23) and the absence of bound Ca^{2+} (dark green, whole complex; magenta, pcdh-15; cyan, cdh-23). **b-c,** Snapshots of the pcdh-15+cdh-23 complex at the end of simulations performed with and without bound Ca^{2+}, respectively. See Supplementary Movies III, IV&V. **d**, Stability of individual EC repeats. RMSD per repeat versus time for simulation of the cdh-23+pcdh-15 complex in the absence of bound Ca^{2+} (SA3; cadherin-23 EC1, blue; cadherin-23 EC2, cyan; protocadherin-15 EC1, violet; protocadherin-15 EC2, magenta). While the complex deformed, individual repeats retained their fold. **e**, RMSD versus time for simulations SA2 and SA4 in the NVT ensemble, shown as in (a).

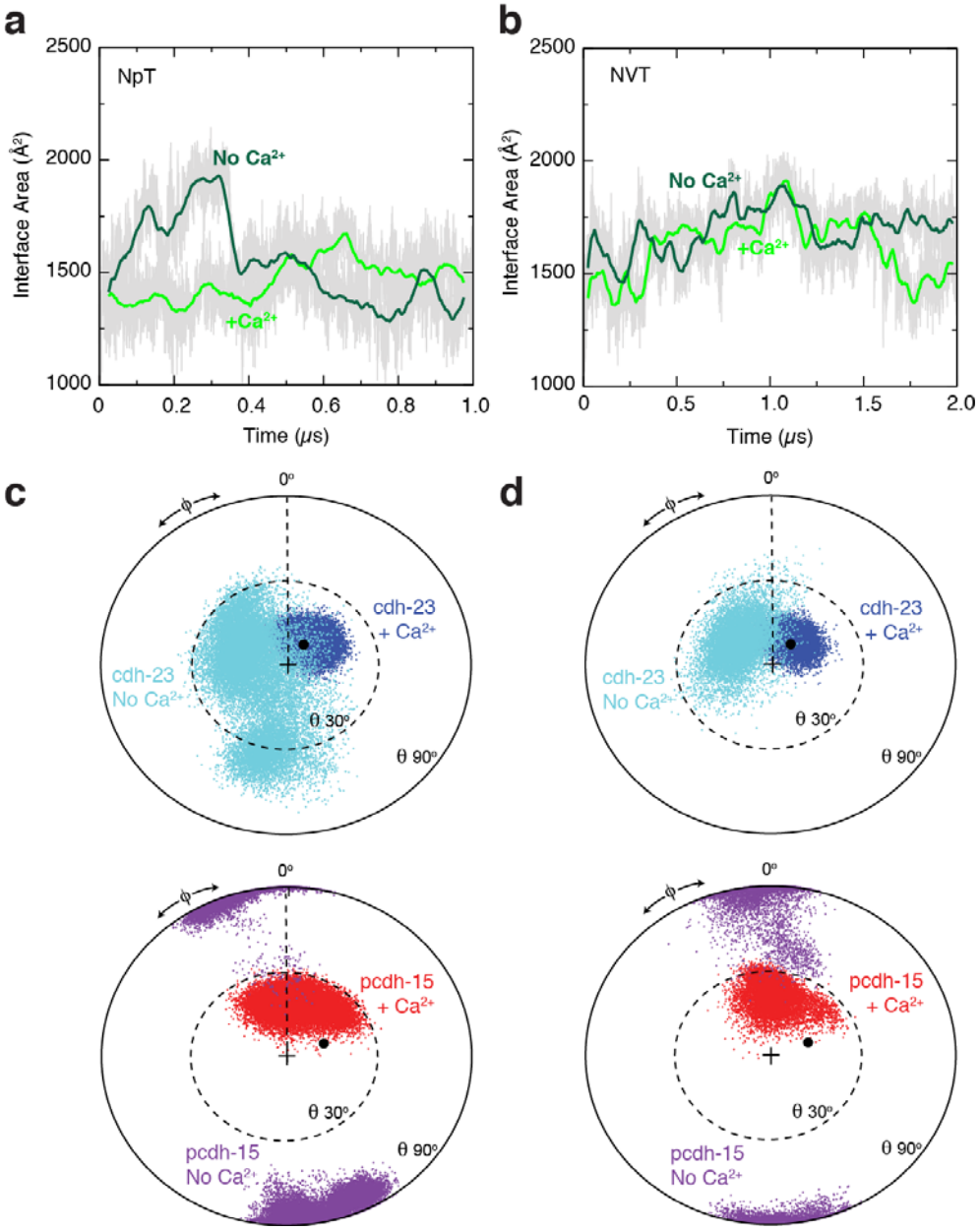

Supplementary Figure 14. Interface area and interrepeat arrangement during simulations with and without bound Ca^{2+}. **a-b,** Surface area of the pcdh-15+cdh-23 interface shown for simulations performed with (light green) and without bound Ca^{2+} (dark green). Simulations SA1 and SA3 in the NpT ensemble are shown in (a), simulations SA2 and SA4 in the NVT ensemble are shown in (b). **c-d,** Conformational freedom of EC2 with respect to EC1 quantified by the projection of the EC2 principal axis into the x-y plane perpendicular to the EC1 principal axis[16]. Vector length relates to the tilt angle (sin θ), while the phase angle corresponds to the azimuthal angle ϕ. Projections are shown for the cdh-23 protomer in the presence (blue) and absence of bound Ca^{2+} (cyan) for simulations SA1 and SA3 (c), as well as simulations SA2 and SA4 (d). Similarly, projections are shown for the pcdh-15 protomer in the presence (red) and absence of bound Ca^{2+} (violet). Black circles highlight initial projections. Both cdh-23 and pcdh-15 display a dramatic increase in inter-repeat motion upon Ca^{2+} removal.

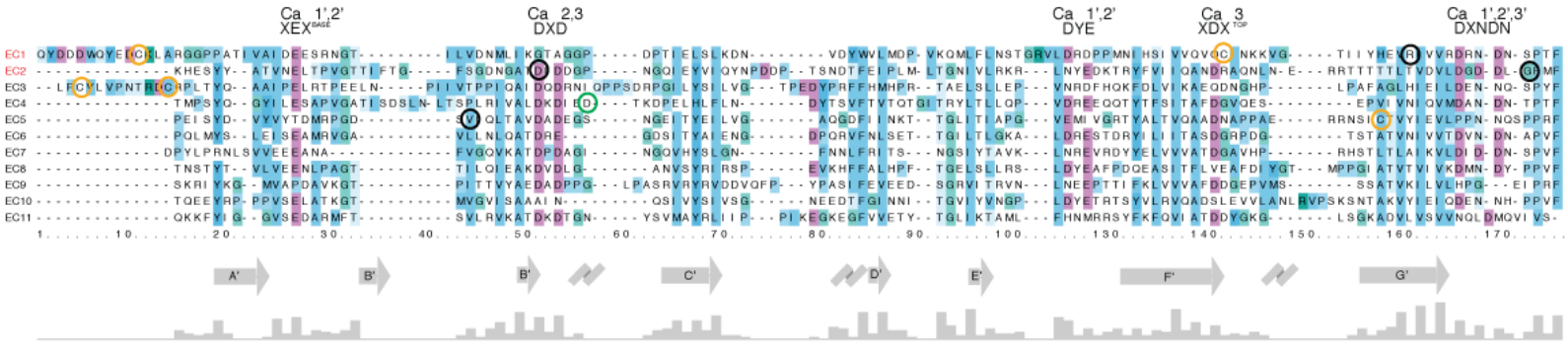

Reference	Mutation Gene #	Structure #	Cadherin Repeat #	Calcium Binding Motif
Ahmed et al. 2003	D139G	D113G	EC1	
Ahmed et al. 2008	D183G	D157G	EC2	**D**XD
Ahmed et al. 2003	G262D	G241D	EC2/EC3	DXNDN**X**
Doucette et al. 2009	V533D	V507D	EC5	
Grossman et al. 2010	D440A	D414A	EC4	

Supplementary Figure 15. Extracellular repeats of human protocadherin-15 and mutations causing hereditary deafness. All 11 extracellular repeats are aligned to each other (EC1 to EC11). Conserved Ca^{2+}-binding sequence motifs are labeled as in Supplementary Fig. 7. Mutations causing hereditary deafness are mapped onto the sequence alignment (top) and listed (bottom) along with their repeat location, reference[27,71,72], and Ca^{2+}-binding motif target. A variant positively selected in East Asians is highlighted in green[67]. Cysteine residues are highlighted in yellow. Secondary structure of protocadherin-15 EC2 and sequence conservation are indicated in gray below the alignment.

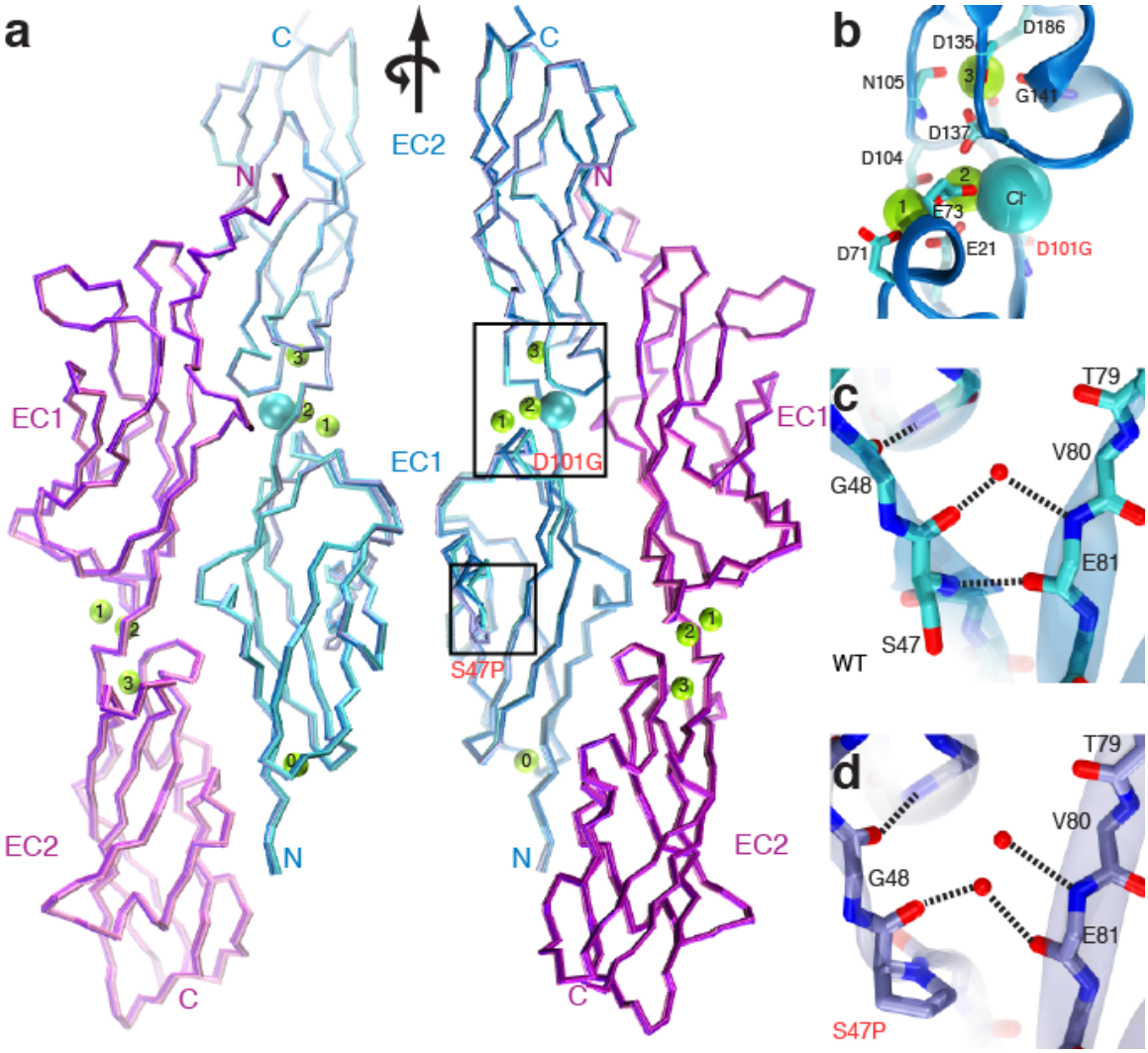

Supplementary Figure 16. Structures of mutant pcdh-15+cdh-23 complexes. **a,** Two views of a superposition of the S1a structure (darker colors) and the two mutant complexes involving cdh-23_{D101G} (S3, cyan) and cdh-23_{S47P} (S4, ice-blue). The three structures were superimposed on the cdh-23 EC2 repeat and shown as C_α traces, with pcdh-15 in purple and cdh-23 in blue. One Cl^- and seven Ca^{2+} ions are shown as cyan and green spheres, respectively. Boxes indicate the approximate position of the details shown in (b-d). **b,** Detail of the cdh-23_{D101G} linker region, with a Cl^- ion bound to Ca^{2+} at binding-site 2^{16}. **c-d,** Detail of interactions between EC1 β-strands C and F for wild-type cdh-23 (S1a) and the cdh-23_{S47P} mutant (S4), respectively. The cyclic side-chain of P47 prevents the formation of a hydrogen bond with the carbonyl oxygen of E81, favoring the separation of both strands by an additional water molecule. Protein backbone and surrounding residues are shown in sticks (cdh-23, cyan; pcdh-15, ice-blue).

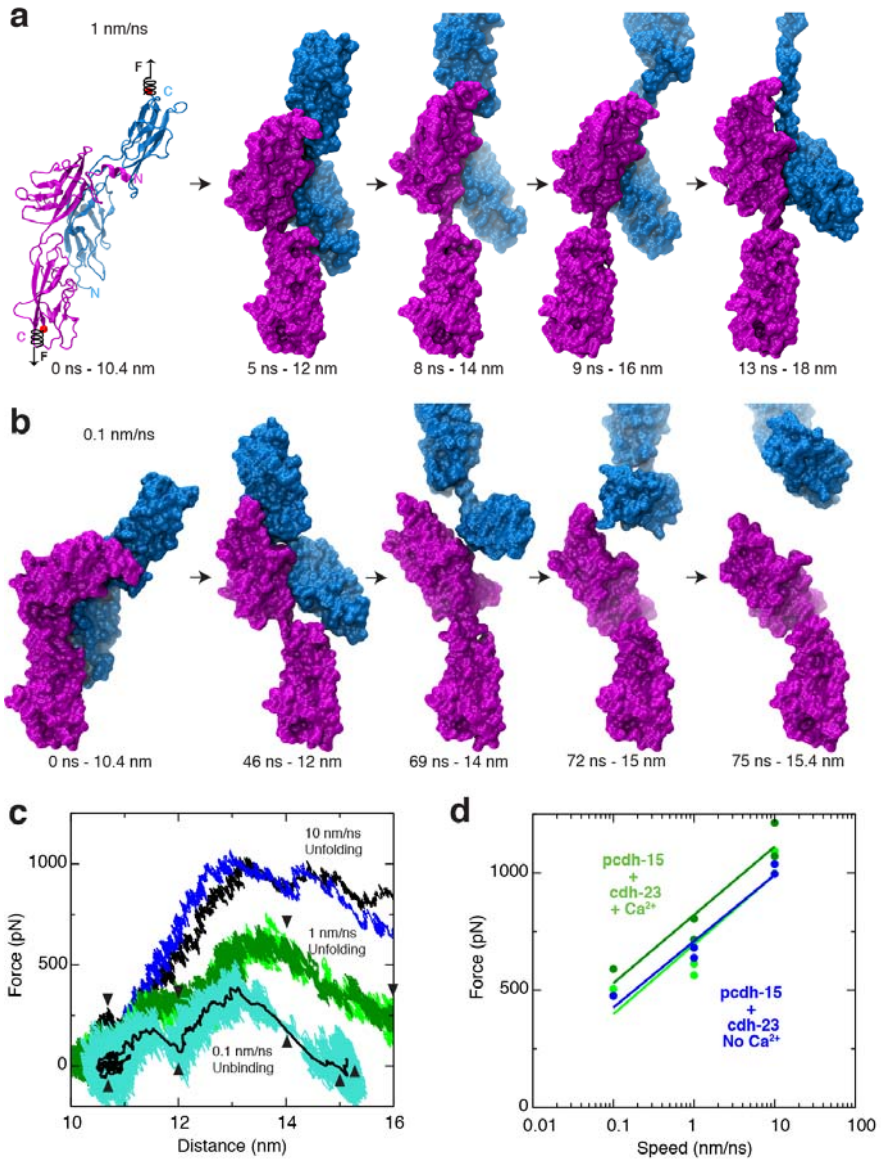

Supplementary Figure 17. Mechanical strength of the pcdh-15+cdh-23 complex probed in the absence of bound Ca^{2+}. **a**, Snapshots of pcdh-15 (purple) and cdh-23 (blue) during simulation SNA11 performed using a stretching speed of 1 nm/ns (Supplementary Table 3). The protein is shown in cartoon representation at the beginning of the simulation, and then in surface representation at indicated time points. The second repeat of cdh-23 unfolded before unbinding of the complex could be observed. **b**, Snapshots of pcdh-15 and cdh-23 as in (a) during simulation SNA13 performed using a stretching speed of 0.1 nm/ns. Complete complex separation was achieved after 70 ns and was preceded by inter-repeat extension (linker unfolding). **c**, Force applied to one C-terminus versus distance between C-termini ends of pcdh-15 and cdh-23. Different traces correspond to independent simulations performed at stretching speeds of 10 (blue and black), 1 (light and dark green), and 0.1 nm/ns (cyan). Snapshots in (a) and (b) are indicated by arrowheads pointing down and up, respectively. A 1-ns running average of the cyan curve is shown in black. Unfolding of an EC repeat preceded unbinding in all simulations except the slowest one. **d**, Maximum force-peak values vs. stretching speed for simulations of the pcdh-15+cdh-23 complex in the absence of bound Ca^{2+} are shown in blue (simulations SNA9 to SNA13). Unbinding forces for simulations with Ca^{2+} (Fig. 3d) are shown in green.

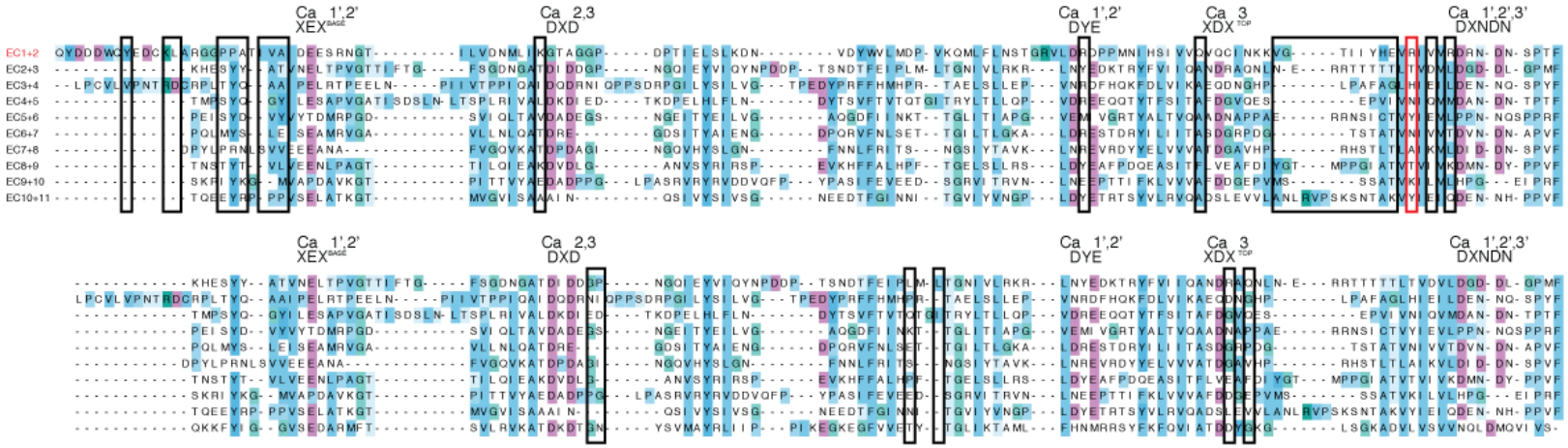

Supplementary Figure 18. Extracellular repeats of human protocadherin-15 and binding interface. All 10 extracellular pairs of repeats are aligned to each other (EC1+2 to EC10+11). Boxes indicate interfacing residues in EC1+2 and equivalent positions throughout the extracellular repeats of protocadherin-15. Position of residue R113 is highlighted in red. Repeats EC6+7 and EC7+8 are most similar to EC1+2 and could be involved in interactions with cdh-23.

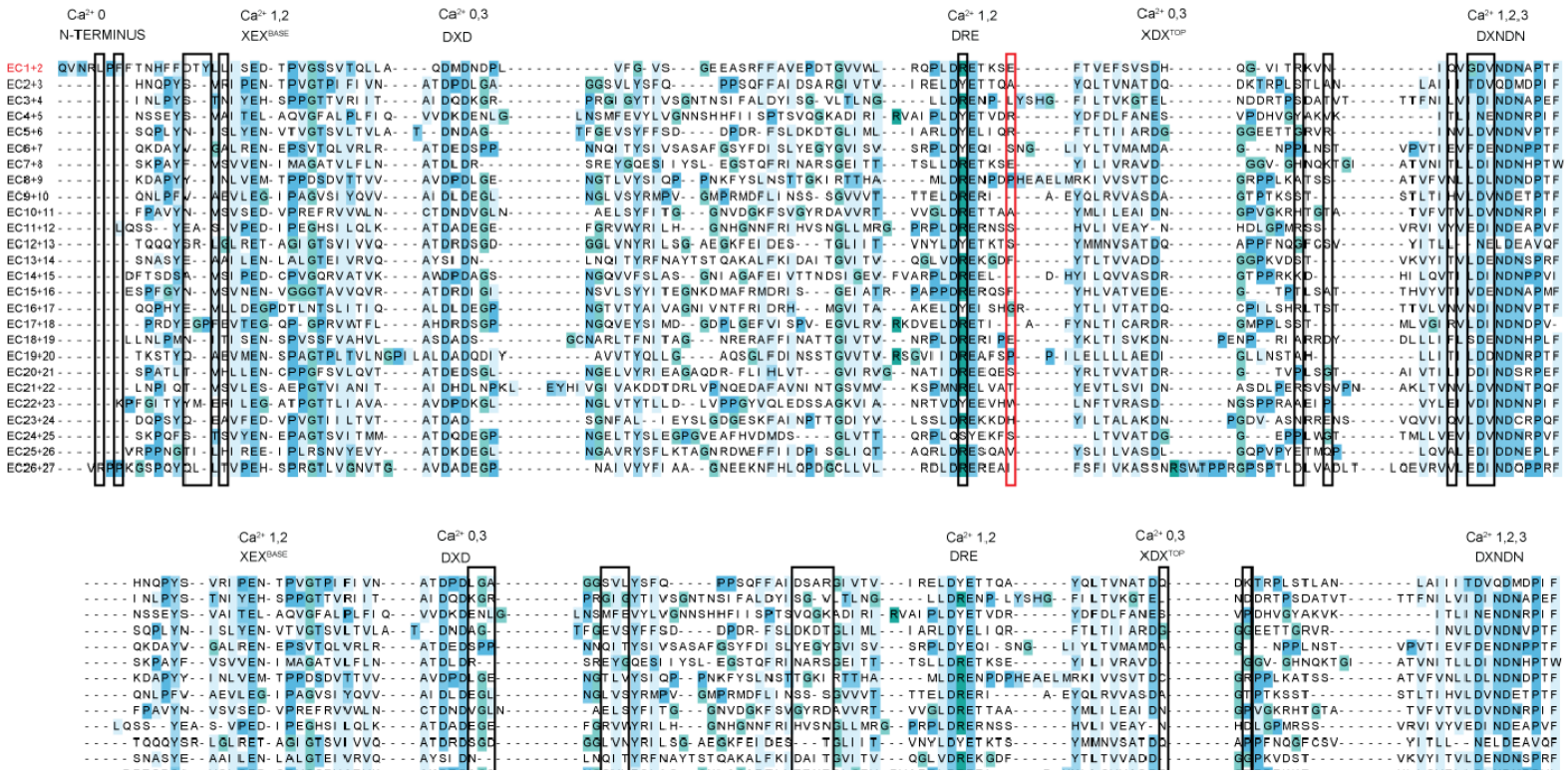

Supplementary Figure 19. Extracellular repeats of human cadherin-23 and binding interface. All 26 extracellular pairs of repeats are aligned to each other (EC1+2 to EC26+27). Boxes indicate interfacing residues in EC1+2 and equivalent positions throughout the extracellular repeats of cadherin-23. Position of residue E77 is highlighted in red. Repeats EC6+7 are the most similar to repeats EC1+2 and could be involved in interactions with pcdh-15.

Supplementary References

50. Harrison, O. J. et al. Two-step adhesive binding by classical cadherins. *Nat. Struct. Mol. Biol.* **17**, 348–357 (2010).

51. Katsamba, P. et al. Linking molecular affinity and cellular specificity in cadherin-mediated adhesion. *Proc. Natl. Acad. Sci. USA*, **106**, 11594-11599 (2009).

52. Brasch, J. et al. Structure and binding mechanism of vascular endothelial cadherin: a divergent classical cadherin. *J. Mol. Biol.*, **408**, 57-73 (2011).

53. Sotomayor, M., Corey, D. P. and Schulten, K. In search of the hair-cell gating spring: elastic properties of ankyrin and cadherin repeats. *Structure*, **13**, 669-682 (2005).

54. Lee, G. et al. Nanospring behaviour of ankyrin repeats. *Nature*, **440**, 246-249 (2006).

55. Li, L., Wetzel, S., Plückthun, A. and Fernandez, J. M. Stepwise unfolding of ankyrin repeats in a single protein revealed by atomic force microscopy. *Biophys. J.*, **90**, L30-L32 (2006).

56. Oroz, J. et al. Nanomechanics of the cadherin ectodomain: "canalization" by Ca^{2+} binding results in a new mechanical element. *J. Biol. Chem.* **286**, 9405-9418 (2011).

57. Corey, D. P. and Hudspeth, A. J. Kinetics of the receptor current in bullfrog saccular hair cells. *J. Neurosci.* **3**, 962-976 (1983).

58. Karplus, M. and Petsko, G.A. Molecular dynamics simulations in biology. *Nature*, **347**, 631-639.

59. Schwander, M. et al. A mouse model for nonsyndromic deafness (DFNB12) links hearing loss to defects in tip links of mechanosensory hair cells. *Proc. Natl. Acad. Sci. USA* **106**, 5252–5257 (2009).

60. Vendome, J., et al. Molecular design principles underlying β-strand swapping in the adhesive dimerization of cadherins. *Nat. Struct. Mol. Biol.* **18**, 693–700 (2011).

61. Pokutta S, Herrenknecht, K., Kemler, R., and Engel, J. Conformational changes of the recombinant extracellular domain of E-cadherin upon calcium binding. *Eur. J. Biochem.* **223**, 1019-1026 (1994).

62. Cailliez, F. and Lavery, R. Cadherin mechanics and complexation: the importance of calcium binding. *Biophys. J.* **89**, 3895-3903 (2005).

63. Vunnam, N., Flint, J., Balbo, A., Schuck, P., and Pedigo, S. Dimeric states of neural- and epithelial-cadherins are distinguished by the rate of disassembly. *Biochemistry* **50**, 2951–2961 (2011).

64. Kim, S. A., Tai, C. Y., Mok, L. P., Mosser, E. A., and Schuman, E. M. Calcium-dependent dynamics of cadherin interactions at cell-cell junctions. *Proc. Natl. Acad. Sci. USA* **108**, 9857–9862 (2011).

65. Vunnam, N. and Pedigo, S. Sequential binding of calcium leads to dimerization in neural cadherin. *Biochemistry* **50**, 2973–2982 (2011).

66. Huertas-Vazquez, A. et al. A nonsynonymous SNP within PCDH15 is associated with lipid traits in familial combined hyperlipidemia. *Hum. Genet.* **127**, 83-89 (2009).

67. Grossman, S. R. et al. A composite of multiple signals distinguishes causal variants in regions of positive selection. *Science*. **327**, 883-886 (2010).

68. Ciatto, C., et al. T-cadherin structures reveal a novel adhesive binding mechanism. *Nat. Struct. Mol.*

Biol. **17**, 339-347 (2010).

69. Boggon, T. J., et al. C-cadherin ectodomain structure and implications for cell adhesion mechanisms. *Science*, **296**, 1308-1313 (2002).

70. Patel, S.D., et al. Type II cadherin ectodomain structures: implications for classical cadherin specificity. *Cell*, **124**, 1255-1268 (2006).

71. Ahmed, Z. M. et al. PCDH15 is expressed in the neurosensory epithelium of the eye and ear and mutant alleles are responsible for both USH1F and DFNB23. *Hum. Mol. Genet.* **12**, 3215-3223 (2003).

72. Doucette, L. et al. Profound, prelingual nonsyndromic deafness maps to chromosome 10q21 and is caused by a novel missense mutation in the Usher syndrome type IF gene PCDH15. *Eur. J. Hum . Genet.* **17**, 554-564 (2009).